BACKGROUND DISCRIMINATION STUDIES AND MEASUREMENTS OF DROPLET AND BUBBLE SIZE FOR THE PICASSO EXPERIMENT

by

NAVARAJ DHUNGANA

A thesis submitted in partial fulfillment
of the requirements for the degree of
Master of Science (M.Sc.) in Physics

The School of Graduate Study
Laurentian University
Sudbury, Ontario, Canada

THESIS DEFENCE COMMITTEE/COMITÉ DE SOUTENANCE DE THÈSE

Laurentian University/Université Laurentienne
School of Graduate Studies/École des études supérieures

Title of Thesis Titre de la thèse	BACKGROUND DISCRIMINATION STUDIES AND MEASUREMENTS OF DROPLET AND BUBBLE SIZE FOR THE PICASSO EXPERIMENT
Name of Candidate Nom du candidat	Dhungana, Navaraj
Degree Diplôme	Master of Science
Department/Program Département/Programme	Physics
Date of Defence Date de la soutenance	December 17, 2013

APPROVED/APPROUVÉ

Thesis Examiners/Examinateurs de thèse:

Dr. Ubi Wichoski
(Supervisor/Directeur de thèse)

Dr. Ian Lawson
(Committee member/Membre du comité)

Dr. Jacques Farine
(Committee member/Membre du comité)

Dr. Alexander J. Wright
(External Examiner/Examinateur externe)

Approved for the Shhool of Graduate Studies
Approuvé pour l'École des études supérieures
Dr. David Lesbarrères
M. David Lesbarrères
Director, School of Graduate Studies
Directeur, École des études supérieures

ACCESSIBILITY CLAUSE AND PERMISSION TO USE

I, **Navaraj Dhungana**, hereby grant to Laurentian University and/or its agents the non-exclusive license to archive and make accessible my thesis, dissertation, or project report in whole or in part in all forms of media, now or for the duration of my copyright ownership. I retain all other ownership rights to the copyright of the thesis, dissertation or project report. I also reserve the right to use in future works (such as articles or books) all or part of this thesis, dissertation, or project report. I further agree that permission for copying of this thesis in any manner, in whole or in part, for scholarly purposes may be granted by the professor or professors who supervised my thesis work or, in their absence, by the Head of the Department in which my thesis work was done. It is understood that any copying or publication or use of this thesis or parts thereof for financial gain shall not be allowed without my written permission. It is also understood that this copy is being made available in this form by the authority of the copyright owner solely for the purpose of private study and research and may not be copied or reproduced except as permitted by the copyright laws without written authority from the copyright owner.

Abstract

The Project in Canada to Search for Supersymmetric Objects (PICASSO) searches for cold dark matter through the direct detection of Weakly Interacting Massive Particles (WIMPs) via spin-dependent and spin independent interactions with ^{19}F nuclei. The detection principle is based on the superheated droplet technique; the detectors consist of a gel matrix with millions of liquid droplets of superheated fluorocarbon (C_4F_{10}) dispersed in it. In order to reduce the background, it is essential to distinguish the signature of different background particles interacting in the detector. A dedicated setup was developed in order to study the response of the C_4F_{10} droplets in the presence of different backgrounds.

The main objectives of this research are to identify the actual size (diameter) of the droplet increases due to phase transition and to check and establish the correlation between the droplet size and the maximum amplitude of the signal. In addition, the alpha-neutron discrimination was studied by observing each event's image frames and the associated acoustic signal to get the amplitude distribution. The mean ratio of bubble size to droplet size was found to be 5.48, independent of temperature and type of interacting particle. Furthermore, no correlation was found between the droplet size and the maximum amplitude of the signal. As for the discrimination studies, the analysis of the signal events has confirmed that alphas generated outside the active liquid in the gel are much more difficult to discriminate from neutron than when alphas are generated inside the active liquid.

Keywords

Dark matter, superheat, droplet, bubble, signal, amplitude, phase transition.

Acknowledgments

First and foremost, I would like to express my sincere gratitude to Dr. Ubi Wichoski for his continuous support, constructive feedback, thoughtful reflection and constant guidance throughout this work. He always encouraged and provided me necessary support. He has been a great source of inspiration on my research. His encouragement and assistance at all times have been of immense value.

I am especially thankful to Dr. Ruslan Podviyanuk for his help and advice in every aspect of the project - from design and experimental set up to data analyses. He always finds spare time to discuss and help me when there are any problems. I am also grateful to Dr. Bharat Pokharel for his valuable help, encouragement and suggestions.

I would like to thank the entire PICASSO team for the discussions which helped me to improve this project. A special thanks to Dr. Viktor Zacek for his valuable suggestions and Mr. Fabrice Debris for preparing the gel.

I am also thankful to Mr. Adam Walli, Mr. Mark Brown and Mr. Tom Fenske for their invaluable help with electronics and equipments. I am especially thankful to Mr. Curtis Laamanen for his invaluable feedbacks on my code and Dr. Oleg Chkvorets for helping with the spikes. A special thanks goes to Dr. Clarence Virtue for providing the neutron source.

I express my hearty gratitude to Dr. Jacques Farine and Dr. Ian Lawson for serving on my committee and providing constructive criticisms and valuable feedback that improved this thesis.

I would like express my indebtedness to all my respected professors of the department of Physics, Laurentian University for making my time at the university fruitful and enjoyable.

I would like to extend the acknowledgement to all my friends especially Suman Neupane, Puskar Raj Chapagain and Dr. Nabin Malakar for their invaluable help in proof reading my thesis.

Last but not least, I like to thank my wife Ambika, son Sijan and daughter Sara for their love, support, patience and encouragement.

Table of Contents

Abstract ..... **iii**

Acknowledgments ..... **iv**

Table of Contents ..... **v**

List of Tables ..... **viii**

List of Figures ..... **ix**

1 Introduction **1**

2 Dark matter **4**

2.1 Observational evidence 4

2.1.1 Rotation curves of spiral galaxies 4

2.1.2 Cosmic Microwave Background 6

2.1.3 Gravitational lensing 7

2.2 Properties of a dark matter particle 9

2.3 Candidates of dark matter 10

2.3.1 Cold Dark Matter 10

2.3.1.1 Axions 10

2.3.1.2 Supersymmetric WIMP 11

2.3.1.3 MACHOs 13

2.4 Detection of dark matter 13

2.4.1 Indirect detection 14

2.4.2 Direct detection 15

2.4.2.1 WIMP-nucleon Interaction 16

2.4.2.2 Interaction Cross-section 19

2.4.2.2.1 Spin-dependent interaction 19

2.4.2.2.2 Spin- independent interaction 20

2.5 Detection techniques and direct detection experiments around the World 21

3 PICASSO 24

3.1 Detection principle 24

3.2 Detector fabrication and installation 28

3.3 Response of background radiation and discrimination 31

3.3.1 Neutron Response 31

3.3.2 Alpha particle Response 33

3.3.3 Gamma Response 34

3.4 PICASSO at SNOLAB 35

3.5 PICASSO results 36

4 Alpha-neutron discrimination 38

4.1 Experimental methods 38

4.1.1 Sound insulation of experimental box 38

4.1.2 Trigger board 39

4.1.3 Experimental arrangement and set up 42

4.1.4 Run details 46

4.2 Data analysis 52

4.2.1 Signal analysis 52

4.2.2 Filters: low pass, high pass, band pass 54

4.2.3 AVar and PVar 55

4.2.4 Power spectrum 56

5 Measurements of droplet and bubble sizes 58

5.1 Method 58

5.2 Ratio of bubble diameter to droplet diameter (R) 59

5.3 Increase of the size of a droplet interacting with background particles 60

5.4 Correlation between a droplet size and maximum amplitude of the signal 66

6 Results 68

6.1 Droplet size distribution 68

6.2 Ratio of bubble diameter to droplet diameter (R) 69

6.3 Correlation between droplets diameter and maximum amplitude of signal 72

6.4 Discrimination between alpha and neutron induced signals 75

6.4.1 Average waveforms and FFT 75

6.4.2 Amplitude distribution 77

6.4.3 AVar 81

7 Discussion and Summary 83

8 References 87

List of Tables

Table 4.1: Runs at temperature 45 ^{o}C used in data analysis 48

Table 4.2: Runs at temperature 40 ^{o}C used in data analysis 49

Table 4.3: Runs at temperature 35 ^{o}C used in data analysis 50

Table 4.4: Runs at temperature 30 ^{o}C used in data analysis 51

Table 4.5: Event rate of good events in alpha and neutron runs..... 52

Table 5.1: Droplet diameter, bubble diameter and maximum amplitude of signal at 30 ^{o}C in alpha run..... 61

Table 5.2: Droplet diameter, bubble diameter and maximum amplitude of signal at 30 ^{o}C in neutron run 64

Table 6.1: Mean ratio of bubble diameter to droplet diameter 70

Table 6.2: Correlation coefficient between droplet size and maximum amplitude of signal . 74

List of Figures

Figure 2.1: The observed rotation curve for spiral galaxy NGC6503. 5

Figure 2.2: Photo of galaxy cluster CL0024+1654 from the Hubble Space Telescope. 8

Figure 2.3: The composite image of the galaxy cluster, also known as the Bullet Cluster..... 9

Figure 2.4: A schematic representation of some well-motivated WIMP-type particles..... 11

Figure 3.1: Threshold energy for ^{19}F recoils as a function of temperature at a pressure of 1.23 bars. 27

Figure 3.2: Normalized detector response to different types of particles as a function of temperature for detector loaded with C_4F_{10} of droplets of 200 μm diameter. 28

Figure 3.3: Current generation of PICASSO detector. 29

Figure 3.4: The inner parts of a TPCS with four detectors. 30

Figure 3.5: Installation of the PICASSO experiment at SNOLAB. 31

Figure 3.6: The response of a SBD loaded with C_4F_{10} response to 200 keV neutrons as a function of temperature 33

Figure 3.7: The normalized α-response of two detectors as a function of temperature..... 34

Figure 3.8: The cosmic-ray muon flux and the muon-induced fast neutron flux as a function of depth. 36

Figure 3.9: Upper limits at 90% C.L. on spin dependent WIMP-proton interactions. PICASSO limits are shown as full lines 37

Figure 4.1: Outside and inside sound and heat insulated experimental box. 39

Figure 4.2: Block diagram of trigger unit showing main parts 40

Figure 4.3: TTL triggering output pulse from comparator, microcontroller algorithm. 41

Figure 4.4: The linear gain of Mitrass amplifier set with gain 55 dB..... 43

Figure 4.5: The time of coincidences between signals and images. 44

Figure 4.6: Block diagram of the experiment to measure the droplet size, bubble diameter and the signal produced due to phase transition. 45

Figure 4.7: Waveform of a typical event due to droplet burst. The blue mark on the waveform shows the fast rise at the beginning of the pulse**.**..... 53

Figure 4.8: One of the examples of strange waveforms observed in clear phase transition raw signal and filtered signal using a high pass (18 kHz) filter..... 54

Figure 4.9: Construction of nRC+ nCR filter, n indicates order of filter. 55

Figure 4.10: The normalized average power spectrum..... 57

Figure 5.1: Experimental design to measure the droplet, bubble diameters and the waveform produced due to phase transitions. 59

Figure 5.2: Reference image frames and Acoustic waveform produced due to droplet burst.60

Figure 6.1: Droplet size distribution in gel samples used in both alpha and neutron runs. 68

Figure 6.2: Droplet size distribution in gel samples in alpha runs and in neutron runs..... 69

Figure 6.3: Mean bubble diameter to droplet diameter ratio at different temperatures. The error bars are at 95% C.L. 70

Figure 6.4: Ratio of bubble diameter to droplet diameter (R) in alpha and neutron runs undergoing phase transitions at different temperatures. 71

Figure 6.5: Variation of droplet diameter with maximum signal amplitude due to phase transitions at 30 ^{o}C..... 72

Figure 6.6: Variation of droplet diameter with maximum signal amplitude due to phase transitions at different temperatures..... 73

Figure 6.7: Average waveforms and FFTs of good events due to phase transitions at different temperatures. 76

Figure 6.8: Amplitude distribution of neutron and alpha particle-induced events 78

Figure 6.9: Amplitude distribution of neutron and alpha particle-induced events 79

Figure 6.10: Amplitude distribution of neutron and alpha particle-induced events 80

Figure 6.11: AVar of neutron and alpha-particle induced events 82

Chapter 1

1 Introduction

Dark matter is one of the greatest unsolved mysteries in cosmology. Approximately 20% of the matter in the universe is known while the remaining 80% is dark matter inferred from the observation of its gravitational effect. Most of the universe's gravitating matter is non-luminous, and its nature and distribution are still unknown. This leads to the concept of dark matter. Research on the nature of dark matter is a challenging topic for scientists in both experimental and theoretical physics. In 1933, astronomer Fritz Zwicky investigated the motion within galaxy clusters. He established evidence for missing mass by observing that the orbital velocity of galaxies within the cluster was higher than what was expected from its luminosity measurements. Nowadays, there is lots of evidence that supports the existence of dark matter. This invisible matter is believed to be constituted of cold, non-baryonic and electrically neutral relic elementary particles named Weakly Interacting Massive Particles (WIMPs); WIMPs have very low interaction cross-sections with ordinary matter. Searching for dark matter may lead to a new understanding of the composition of the universe and the physics behind it. Recently, many experiments have focused on searching for dark matter. The Project in Canada to Search for Supersymmetric Objects (PICASSO) is one of those experiments, located at SNOLAB, a laboratory 2 km underground, near Sudbury, Ontario.

PICASSO is an experiment that searches for cold dark matter by attempting to directly detect WIMPs, primarily via spin-dependent (and spin-independent) interactions with ^{19}F nuclei. The detection principle is based on the superheated droplet technique; the detectors consist of a gel matrix with millions of liquid droplets of superheated fluorocarbon (C_4F_{10}) dispersed within. Neutron interactions, as well as WIMP interactions, in the superheated (metastable) C_4F_{10}, may cause ^{19}F nuclei to recoil and produce a heat spike. The heat deposited this way may trigger an explosive phase transition that is acoustically detected by piezoelectric sensors attached on the walls of the acrylic containers. The background is dominated by alpha particles stemming from

radioactive contamination inside the detector: alpha particles deposit energy continuously as they traverse the superheated liquid. As a result, they may produce many heat spikes that can trigger a phase transition. In order to reduce the alpha particle background, one option is to recognize its acoustic signature, which is expected to be different from the neutron (or WIMP) signature, and discriminate against it [1]. The entire experiment is shielded with water to protect the detectors from neutrons coming from the surrounding rock and shotcrete in the laboratory. The detectors are insensitive to gamma rays and electrons in the operating range of temperature (20-50^{o} C), which is the one of main advantages of the PICASSO detectors [1].

The main objective of this thesis was to study the detector's response to neutrons and alpha-particles, and to try and discriminate between the acoustic signal produced by events induced by neutron and by events induced by alpha-particles. Hence, a dedicated setup was developed in order to study the response of C_4F_{10} droplets in the presence of alpha and neutron interactions. Small samples of the PICASSO detector's gel spiked with alpha emitting contaminants (alpha runs) and non-spiked gel irradiated by a neutron source (neutron runs) were studied. The size (diameter) of the droplets and the corresponding bubbles due to phase transition were measured, and the ratios of the bubble size to the droplets size at different temperatures were calculated. The correlation between the size of the droplet and the maximum amplitude of the signal due to phase transition were studied, and the relation between these two variables is presented. Finally, the amplitude distribution of neutron and alpha-particle induced events at different temperatures was studied, and compared with previous results [1].

Dark matter, information about its evidence, possible candidates, detection techniques and dark matter search experiments around the world are discussed in Chapter 2. A detailed description of the PICASSO experiment, including detectors, the detection principle and detector's installation is discussed in Chapter 3. The response of small detector gel samples to neutrons and alpha-particles at different temperatures is analyzed in Chapter 4. In Chapter 4, a detailed description of the experimental apparatus used to study alpha-neutron discrimination is presented. In Chapter 5, the size of the droplets and its corresponding bubble, as well as the correlation between droplet size and the

maximum amplitude of the signal due to phase transitions, are investigated. The results of the experiment are presented in Chapter 6. A discussion of the results, summary and conclusion of the thesis are presented in Chapter 7.

Chapter 2

2 Dark matter

2.1 Observational evidence

In 1933, Fritz Zwicky postulated the concept of dark matter to account for the evidence of missing mass by studying the orbital velocities of galaxies in the great Coma cluster. The discrepancies in the results between the calculated mass of cluster based on the orbital velocity of its galaxies and mass of the cluster based on its total light output give the evidence of unseen mass [2]. The evidence of the existence of dark matter includes the observation of the rotational speed of spiral galaxies, the gravitational lensing of background objects, and the observed fluctuation in the cosmic microwave background radiation. All the evidence to support the existence of dark matter is indirect. To solve this missing mass problem, it is necessary to confirm the existence of dark matter by direct detection; physicists are headed in this direction.

2.1.1 Rotation curves of spiral galaxies

Rotation curves of spiral galaxies are the observational tools used to determine the amount of gravitational mass in spiral galaxies. They provide fundamental information for understanding the dynamics, evolution, and formation of spiral galaxies. The circular velocities of clouds of neutral hydrogen can be measured as a function of the distance from the centre of galaxies (r). The data for rotation curves for our galaxies have been sourced from the study of radio emission from hydrogen gas [3]. This data shows that the rotational speed of objects does not decline towards the edge of the galaxy, as expected, but the curve is flat out to the edge of the observable galaxy. In other words, initially velocity rises near r = 0, and remains constant as far as it can be measured. This implies (from Newtonian law) that galaxies are immersed in dark matter haloes, with $\rho(r)$ proportional to r^{-2} and hence M(r) proportional to r, far from the centre of galaxy. In

principle, it is expected that once r becomes greater than the extent of mass, the velocity should decline, from Newtonian dynamics,

$$v(r) = \sqrt{\frac{GM(r)}{r}} \tag{2.1}$$

where G is the universal gravitational constant, and M(r) is the mass enclosed by the orbit of radius r, and is given by

$$M(r) = 4\pi \int \rho(r) r^2 dr \tag{2.2}$$

where ρ(r) is the density of the contained mass, but this is not observed, and indicates the existence of the extended dark halos around the spirals galaxies [4].The rotation curve for a typical spiral galaxy is shown in figure 2.1.

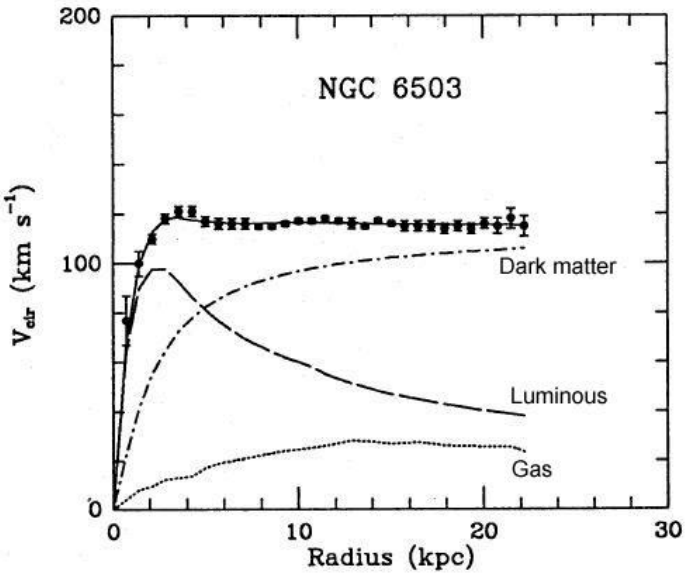

Figure 2.1: The observed rotation curve for spiral galaxy NGC6503. The prediction curve from the dark matter halo, the visible galactic disk and hydrogen gas surrounding the galaxy are shown by dash-dotted, dashed and dotted lines respectively [5].

It is seen that the luminous disk does not extend further than 5 kpc from the centre of the galaxy. If the matter is all there, the rotation curve would drop at larger radii. From the discrepancy between the observed rotation curve and the rotation curve due to the

luminous disk and gas, we infer the existence of a dark halo. Moreover, the rotation curve of NGC 3198 implies $\Upsilon > 30h\Upsilon_{\odot}$ or $\Omega_{halo} > 0.017$ whereas the density of luminous matter, $\Omega_{lum} = 0.003h^{-1} = 0.0041$, where Υ is the mass to light ratio, $\Upsilon_{\odot}$ is the mass to light ratio of sun and h is the present day normalized Hubble expansion rate [6]. The large discrepancy between these numbers seen in many external galaxies provides the most robust evidence for dark matter.

2.1.2 Cosmic Microwave Background

One of the successes of the Big Bang Theory is its prediction of the almost perfect black body spectrum and its detailed prediction of the anisotropies in the Cosmic Microwave Background radiation. The recent Wilkinson Microwave Anisotropy Probe (WMAP) has precisely measured these anisotropies over the whole sky. These anisotropies are the results of characteristic density perturbations at the time of recombination of electron and proton and give us insight into the density of matter and energy in the Universe. It is useful to define each component of the Universe (radiation (r), matter (m), and dark energy (Λ)) relative to the critical density, ρ_c. The critical density is defined as,

$$\rho_c = \frac{3\,H^2(t)}{8\pi G} \tag{2.3}$$

where H (t) is the Hubble parameter and is defined as the ratio of recession velocity of a galaxy to its distance from the observer. The relative abundance, Ω_i, of the i^{th} (i = r, m, Λ) constituent of the Universe with a density of ρ_i can be expressed as,

$$\Omega_i = \frac{\rho_i}{\rho_c} \tag{2.4}$$

The newly released WMAP data are sufficiently sensitive to test dark energy, providing important new information. The new WMAP data, together with the current expansion rate of the Universe and the large scale galaxy distributions, provides a measurement of the relative abundances of baryonic matter, dark matter, and dark energy [7].

2.1.3 Gravitational lensing

Gravitational lensing observations give a lot of evidence of dark matter. Gravitational lensing exploits the fact that light is bent by the gravitation of massive objects in a manner similar to the optical refraction, it is explained in the framework of Einstein's Theory of General Relativity. From this theory, it can be understood that the gravitational fields of massive objects cause light rays passing close to that object to be bent and refocused somewhere else. The more massive the object, the stronger its gravitational field, which leads to an increased bending of light rays. This is analogous to the larger deviation of the incident light in an optical lens, with material having a higher index of refraction.

To explain how gravitational lensing works, let us consider a bright source, a massive object, and an observer in a straight line. The deformation of the light from a source such as a galaxy or a star into a ring through gravitational lensing of the source light by an object with an extremely large mass such as another galaxy is called an Einstein ring. The observer sees an Einstein ring of the light source. However, if the gravitational lens does not lie along the central line of view (as found commonly in the respective distance between the light paths), it results in multiple distorted images, as shown in figure 2.2 below. Careful analysis of this distortion allows an understanding and a determination of the distribution of mass that produced the gravitational lens. Commonly, the huge dark matter concentrations in clusters of galaxies creates typical bending angles of 30 arc seconds, and highly distorted multiple images of a fortuitously aligned background source galaxy. In modern cosmology, this is the most valuable tool to study the components of matter in a galaxy cluster. Many projects searching for unknown mass in the cluster, namely Cosmic all Sky Survey (CLASS), Optical Gravitational Lensing Experiment (OGLE), and Microlensing Observations in Astrophysics (MOA) use this technique. The CLASS estimated the total matter density of $\Omega_m = 0.31^{+0.27}_{-0.14}$ using the method of gravitational lensing [8].

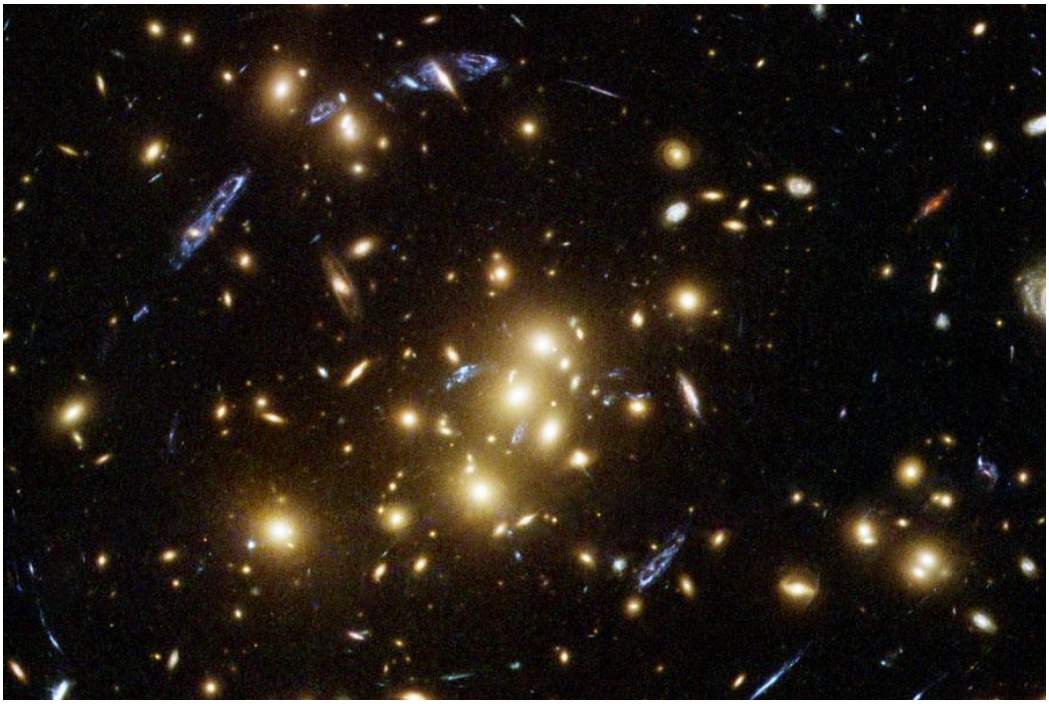

Figure 2.2: Photo of galaxy cluster CL0024+1654 from the Hubble Space Telescope. Cluster galaxies appear yellow and, together with the cluster's dark matter, acts as a gravitational lens [9].

The NASA Chandra X-ray Observatory found evidence of dark matter using the gravitational lensing technique. The blue area in figure 2.3 represents most of the mass of the clusters. The concentration of this mass is determined by using the gravitational lensing technique, where the light from distant objects is distorted by intervening matter. The hot gas in each cluster is slowed down by a drag force similar to the air resistance during collision. However, dark matter is not slowed down as much by the collision, as it does not interact directly with itself or the gas (except for gravity). In this process, the dark matter components of galaxies have effectively passed through one another without changing much. On the other hand, the hot gas made of the normal baryonic matter has collided and slowed down (shown in pink).

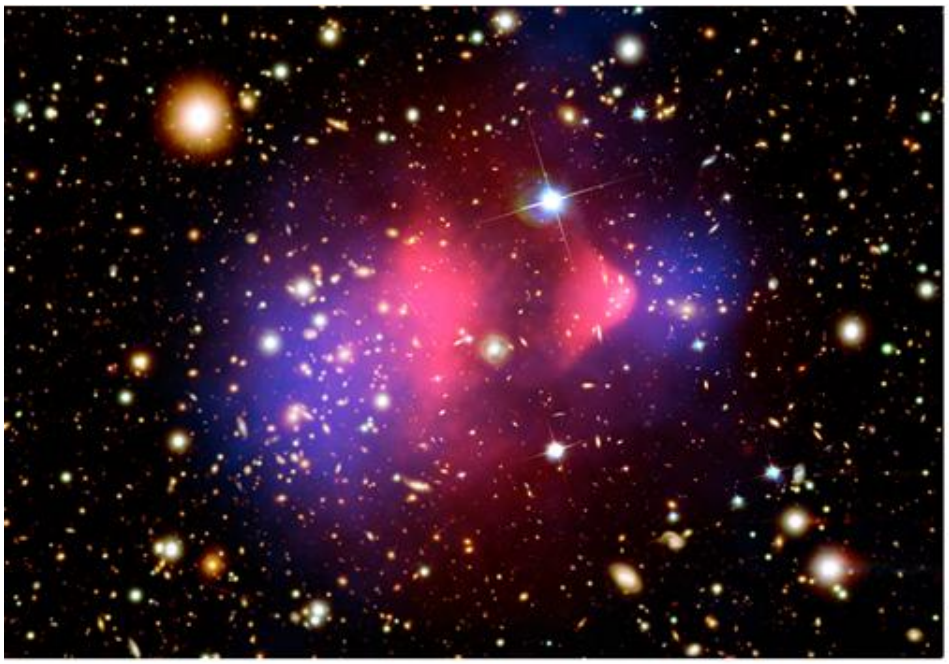

Figure 2.3: The composite image of the galaxy cluster, also known as the Bullet Cluster. The distribution of dark matter inferred from gravitational lensing is shown in blue. The baryonic material that exists as hot gas was determined from X-ray emissions; it is shown in pink, whereas the distribution of visible material can be seen in white (Hubble Space Telescope) [10].

2.2 Properties of a dark matter particle

Dark matter neither emits nor absorbs light or other electromagnetic radiation. Its existence is inferred from its gravitational effects on visible matter, gravitational lensing, and radiation; it was originally hypothesized to account for discrepancies between the calculations of the mass of the galaxies, the clusters of the galaxies, and the large scale structure of the universe.

The main property of these hypothetical dark matter particles is listed as follows: should be non-baryonic. Recent observations, including the WMAP results [11], reveal that a majority of the mass of the universe exists as non-baryonic matter that has not yet been detected. Moreover, the Big Bang Nucleosynthesis presents an upper limit of approximately 5% for the amount of baryons in the universe [12]. Based on all these

explanations, it can be inferred that the dark matter particle should be non-baryonic. Since the dark matter does not emit, reflect or absorb light, it should be insensitive to the electromagnetic force and interact primarily through the gravitational force only. It is also expected to interact hardly with ordinary matter through weak interaction.

Further, dark matter particles should be cold and non-relativistic dark matter at the time of this decoupling from the cosmic plasma in order to allow for the currently observed structure of the universe and the clumping of galaxies into clusters. The upper limit on the contribution of light neutrinos to the density of non-baryonic matter is $\Omega_{\upsilon} \leq 0.014$ (95% C.L.), suggesting that cold dark matter must form the dominant component.

2.3 Candidates of dark matter

2.3.1 Cold Dark Matter

2.3.1.1 Axions

Axions are a well-motivated dark matter candidate, much lighter than the Supersymmetry (SUSY) relics and produced by a very different mechanism. Axions and SUSY relics behave as cold dark matter and cluster effectively to form galaxies and large scale structures [13]. Axions were postulated to explain the lack of CP violation in the strong interaction [14]. In the early universe, axions could be produced by two distinct mechanisms. At the QCD phase transition, the transition at which free quarks are bound into hadrons, a Bose condensate of axions form and these very cold particles would naturally behave as cold dark matter. Secondly, axions can be produced through the decay of strings formed at the Peccei-Quinn phase transition [15].

The properties of the axion are basically set by its mass (m_a), which is inversely proportional to the scale of Peccei-Quinn symmetry breaking. The chances of coupling of axions with protons and electrons are high if the mass is small. Raffelt using astrophysical arguments constrained, $m_a < 10^{-2}$ eV [16]. On the other hand, if the axion had a larger mass, then it would have had an observable effect on stellar evolution and on

the dynamics of SN 1987A. That means the axion mass should be in the range of a few μeV to a few meV. A detailed discussion of axion search experiments and current limits on the axion mass and interaction strength can be found in [17].

2.3.1.2 Supersymmetric WIMP

A WIMP called the Neutralino is a hypothetical particle; it is predicted to exist in supersymmetry theory, and it is considered as one of the main candidates for cold dark matter. It is assumed that the mass of the WIMP lies between 10 GeV to a few TeV. The interaction cross-section of the WIMP lies in the order of weak interaction scale. There are a number of WIMP-type candidates in various theories, shown in figure 2.4.

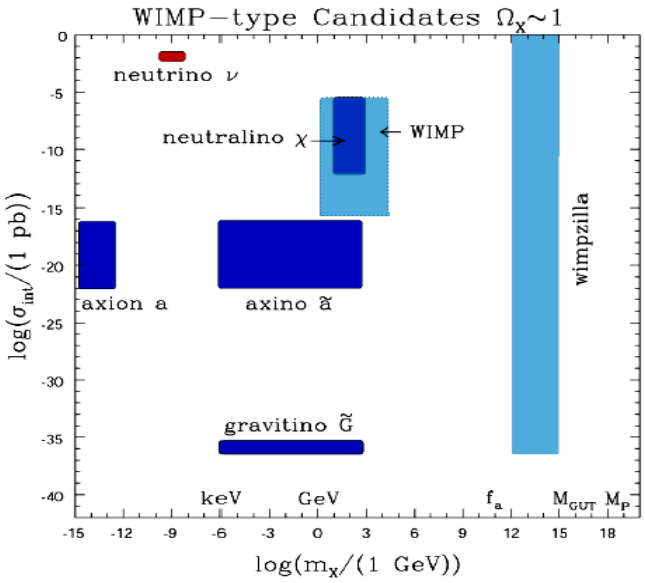

Figure 2.4: A schematic representation of some well-motivated WIMP-type particles showing interaction strength with ordinary matter versus mass of various WIMP-type particles. It should be noted here that the area labeled WIMP covers several possible candidates, one of which is the neutralino [18].

These candidates have not been simply invented as possible solutions to the dark matter problem, but have independently been predicted by the Standard Model and SUSY.

The currently available data in elementary particle physics can be accounted for by a theory called the Standard Model (SM), in which matter is made of quarks (the building blocks of protons and neutrons) and leptons (including electrons and neutrinos), while the strong, weak and electromagnetic forces are mediated by particles like the photon. However, the Standard Model does not predict the existence of any particle that might be dark matter, e.g. neutralino (χ).

The idea of supersymmetry was developed to solve many problems in particle physics that could not be explained by the Standard Model. Most versions of supersymmetry predict the existence of a stable weakly interacting massive particle that would be a natural candidate for dark matter. Dark matter made up of WIMPs would be cold dark matter.

Supersymmetry is a hypothetical idea that imposes a new symmetry onto known classes of particles i.e. bosons and fermions. The bosons, such as the photon, are responsible for carrying the known forces. The fermions include the atomic building blocks, i.e. the proton, neutron, electron, quarks, leptons; according to supersymmetry, for every type of boson in the universe, there must also be a corresponding fermion and vice-versa.

The relation between the supersymmetry and dark matter is the conservation of a quantum number called R-parity. The ordinary particles (Standard Model) all have R-parity equal to +1, while the SUSY particles all have R-parity of -1 or R-odd. Thus, heavier super partner particles can decay into lighter ones whereas the lightest superpartner (LSP) must be stable as there is no lighter negative R-parity particle into which it can decay and it is a natural candidate for dark matter. The R-parity of any particle is given by the relation,

$$R = (-1)^{L+3B+2S} \tag{2.5}$$

where L, B and S are its lepton number, baryon number and spin respectively. The LSP is the spin-1/2 particle called the neutralino, which is its own antiparticle and is actually a

linear combination of the superpartners of the photon, the Z^o boson and two Higgs bosons [19].

The neutralino, χ, is the best favored WIMP candidate amongst dark matter search experiments. Numerous collaborations around the world have been developed to detect the χ by indirect or direct detection methods based on several different detection principles.

2.3.1.3 MACHOs

The term Massive Astrophysical Compact Halo Objects (MACHOs) can be used to include numerous examples of massive astronomical bodies emitting little or no light such as brown and white dwarfs, neutron stars, stellar black holes, a class of sub-stellar objects; hydrogenous comet like-bodies, snowballs and large planets that have ended up orbiting the galaxy. The MACHO collaboration claimed that using microlensing to predict the existence of many MACHOs with average mass of about 0.5 $M_\odot$. This is enough to make up 20% of the dark matter in the galaxy. However, recent data from the Hubble Space Telescope suggest that the dark halo is about only $\leq$ 5% white dwarfs [20]. These rules out the possibility that invisible baryonic matter in the form of MACHOs could account for a significant percentage of the dark matter present in spiral galaxies; hence, the missing mass problem is not solved by MACHOs.

2.4 Detection of dark matter

The dark matter particles, like the neutralino, can be searched either through the detection of signals from its direct interaction with ordinary matter or indirectly, through the observation of its annihilation products, such as high–energy neutrinos, positrons and gamma rays. There are advantages and disadvantages associated with the direct and indirect methods; however, the development and improvement of detectors of both types will give us a greater chance of detecting dark matter. Unfortunately, the direct and indirect searches for dark matter particles have so far all given either negative or contradictory results. So far, to the best of our knowledge, no verified detection of dark

matter has been made, but the properties of the dark matter particles have been understood and increasingly improved over time.

2.4.1 Indirect detection

Indirect detection of dark matter is based on the technique of observing the radiation produced in dark matter annihilations. The flux of such radiation is proportional to the annihilation rate, which depends on the square of dark matter density i.e.

$$\Gamma_{Ann} \propto \rho_{\chi}^{2} < \sigma_{Ann}(v_{rel})v_{rel} > \tag{2.6}$$

where ρ_{χ} is the dark matter density, σ_{Ann} is the neutralino-neutralino annihilation cross-section and v_{rel} is the relative speed of two annihilating neutralinos. Thus, the natural places to search for significant fluxes are the regions where a larger proportion of dark matter accumulates, such as the sun, the earth, the galactic centre, and dwarf spheroidal galaxies [21].

Neutrinos could give an interesting signature as dark matter particles scatter in the interior of the sun or earth and, due to gravitation, are trapped there, increasing the number density and hence the annihilation rate. The annihilation rate is quadratic in the number density of dark matter particles. Standard Model particles are created due to dark matter annihilations. Neutrinos escaping from the solar core can be recorded using suitable detectors on earth. The energy of these types of neutrinos is roughly between $\frac{1}{3}$ to $\frac{1}{2}$ of the mass of the WIMPs. These neutrinos are much more energetic than the solar neutrinos from nuclear reactions that have already been detected. As a result, the higher energy neutrinos from this WIMP annihilation can be easier to detect than ordinary solar neutrinos. These high energy neutrinos emitted from the centre of the sun and earth would be taken as evidence for WIMP dark matter. The discovery of energetic neutrinos from the direction of the sun would be a spectacular verification of this process and the mass of the dark matter particle could then be roughly estimated. The current large

neutrino telescopes like Ice cube [22] and ANTARES [23] have dark matter research capabilities.

As γ-rays have several unique properties, most studies of indirect detection have been looking for γ-rays from dark matter annihilation: γ-rays do not scatter appreciably during their travel through the galaxy; rather, they point back to the site where the annihilation took place. γ-rays produced by WIMP annihilations have higher energies in the range of GeV or TeV. At these energies, photons interact with matter through $e^+ e^-$ pair production, and will have an interaction length of approximately 38 g/cm^2, which is much shorter than the thickness of Earth's atmosphere at 1030 g/cm^2 [24]. So the direct detection of γ-rays with these energies requires space-based detectors, such as the Fermi Gamma-ray space telescope launched in 2008 [25], which is formally known as the Gamma-ray Large Area Space Telescope (GLAST). Also, indirect detection of γ-rays produced by WIMP annihilation can be achieved in ground-based observatories by detecting secondary particles and Cherenkov light produced by the interaction of photons in Earth's atmosphere. VERITAS [26] and CANGAROO [27] collaborations use an array of multiple 10-12 m optical telescopes that probe the sky for air showers of Cherenkov radiation that can be used to pinpoint sources of high energy γ-rays in the galaxy. These telescopes can be used to detect dark matter annihilation by measuring an excess of γ-rays being emitted by a source like the galactic core, which cannot be attributed to normal γ-ray production by visible matter alone.

Indirect dark matter detection via annihilation in the galactic centre region is an exciting possibility, although the prospects for the observation of γ-rays, neutrinos, and synchrotron radiation from that direction strongly depend on astrophysical parameters, such as the profile of dark matter in the innermost regions.

2.4.2 Direct detection

Direct detection of dark matter particles appears as one of the most promising techniques. The idea is based on the fact that, 'if the galaxy is filled with WIMPs, many of them should travel through the solar system and traverse the earth with typical galactic

velocities of ~ 220 km/sec i.e. with $\frac{v}{c} \sim 10^{-3}$, making it possible to look for the interaction of such particles with matter' [28].There is a chance to observe such interactions since dark matter is part of our own galaxy where it is more or less smoothly distributed. It is therefore expected that the dark matter particles will cross the path of Earth and interact with the detectors.

In the calculation of the signal in direct detection experiments, the local density (ρ), the velocity distribution of WIMPs in the solar neighborhood, and the WIMP-nuclear scattering cross section (σ) are paramount. For a given value of ρ and σ, the rate of events expected in an experiment per unit time, per unit detector mass can be determined.

2.4.2.1 WIMP-nucleon Interaction

It has been already mentioned that the direct WIMP detection rate for an underground detector depends on several factors, such as the local density of WIMPs near Earth, the velocity distribution of WIMPs in the Milky Way (Maxwell's distribution), and the cross-section of target nuclei. M.W. Goodman and E. Witten proposed the direct detection of WIMP dark matter in 1985. A number of direct detection experiments are currently underway. The main aim of these experiments is to detect or set limits on nuclear recoils arising from collisions between the WIMPs and the target nuclei. For this purpose, different target materials are used. We will review the mathematical frameworks of the direct detection of dark matter in detail in this section, based on the work pioneered by J.D. Lewin and P.F. Smith [28].

The WIMPs traversing the detector volume will undergo a weak interaction with one of the detector nuclei, causing the nucleus to recoil and produce a detectable signal. Most experiments are based on observations of ionization (charge), scintillation (photons), low temperature phonons (heat), or combinations of some of these. They all have a common basic theoretical interpretation. The typical differential energy spectrum of WIMP-nuclear recoils in a direct WIMP search detector (for the simplest case of a stationary detector in the Galaxy) is,

$$\frac{dR}{dE_R} = \frac{R_0}{E_0\, r} e^{-\left(\frac{E_R}{E_0\, r}\right)} \tag{2.7}$$

where R is the event rate, E_R is the recoil energy, and E_0 is the most probable or mean incident kinetic energy (K.E.) of a dark matter particle of mass M_χ, R_0 is the total event rate, and r is the kinematic factor that is given by,

$$r = \frac{4M_\chi M_T}{(M_T + M_\chi)^2} \tag{2.8}$$

where M_T is the mass of target nucleus. Given that typical WIMP galactic velocities are of order 10^{-3}c, and that WIMP mass estimates lie in the range of 10-1000 $GeVc^{-2}$, it is expected that the recoil energies from WIMP-nuclear interaction would be in the range 1-100 keV [28].

The WIMP energy spectrum can be derived from the right hand side (rhs) of equation (2.7). Practically, the rhs of equation (2.7) is complicated; we need to take into account the following (various) corrections. We will discuss some of these factors in detail in the next section.

I. The detector is not stationary as Earth is in orbit around the Sun, which is moving through the galaxy.
II. The detection efficiency for nuclear recoils and electron recoils could be different. So, the true recoil energy will differ from the observed recoil energy. In this context, a quenching factor needs to be taken into account.
III. The target may consist of more than one element (currently COUPP uses CF_3I which is contains more than one target element in the detector). So each element/species requires separate calculations for WIMP-nucleon cross-section limits.
IV. The resolution and threshold effects limit the capability of every experiment.
V. The predicted interaction cross-sections differ for spin-dependent and spin independent interactions (For detail explanations see 2.4.2.2).
VI. A form factor correction, which is due to the finite size of the nucleus and depend on the nuclear radius and the recoil energy, should be considered.

To take account of these consideration, equation (2.7) can be rewritten as,

$$\frac{dR}{dE}\Big|_{observed} = R_o S(E) F^2(E) I \tag{2.9}$$

where S is the modified spectral function that includes the factors (I-IV), listed above, F is the form factor correction which is an intuitive and simple tool used to describe the scattering particles from extended targets. The detailed explanation about S and F can be found in [28]. I is an interaction function involving spin-dependent and/or spin – independent factors (V). R_0 remains the unmodified rate for a stationary Earth/a static detector, which can be estimated from the observed differential spectrum. The normalized value of R_0 with $\rho_\chi = 0.3$ GeVc^{-2}cm^{-3}, a mean dark matter particle velocity, $v_0 = 230$ kms^{-1} assuming zero momentum transfer cross section σ = constant (σ_0) and the Earth's velocity relative to dark matter distribution, $v_E = 0$ is given by,

$$R_o = \frac{405}{M_\chi M_T}\left(\frac{\sigma_0}{1pb}\right)\left(\frac{\rho_\chi}{0.3\ GeVc^{-2}cm^{-3}}\right)\left(\frac{v_0}{230\ Kms^{-1}}\right) \text{ (kg}^{-1}\text{ day}^{-1}\text{)}$$

where M_χ and M_T are in GeVc^{-2} and $M_T = 0.932$ A is the mass of target nucleus, with A the atomic mass of the target atom.

The recoil energy of a nucleus struck by a dark matter particle of kinetic energy $E = \frac{1}{2}M_\chi v^2$ is given by,

$$E_R = E_0 r(1 - cos\theta) \tag{2.10}$$

where θ is the scattering angle in the centre of mass frame, r is the kinematic factor, and E_0 is the most probable incident kinetic energy of dark matter particle and is given by,

$$E_0 = \frac{1}{2}M_\chi v_0^2 = \frac{v_0^2}{v^2}E \tag{2.11}$$

where v is the velocity of WIMP.

2.4.2.2 Interaction Cross-section

In experiments involving the direct detection of dark matter, the cross-section for elastic scattering of a WIMP from ordinary matter is its most important property. The detection rate in the direct detection experiment is determined by this cross-section. It determines also the rate at which particles from the galactic halo accrete into the Earth and Sun and hence determines the signal in the indirect detection experiment. The interaction of dark matter particles with nuclei of ordinary matter is of electro-weak strength expressed through the elastic scattering cross-section, σ_A and is given by,

$$\sigma_A = 4G_F^2 \mu_A^2 C_A^2 F(q^2) \tag{2.12}$$

where G_F is the Fermi coupling constant, $\mu_A = \frac{M_\chi M_T}{M_\chi + M_T}$ is the reduced mass of neutralino/WIMP and target nucleus, C_A is an enhancement factor that carries all the particle-physics model information and that is dependent on the nucleus and type of WIMP interactions, and $F(q^2)$ is a nuclear form factor that becomes important for large mass number, A and momentum transfer, q. Generally, many forms of interactions exist and all contribute to the total cross-section. The dominant interaction types to consider are: Spin-dependent interaction and Spin-independent interaction. However, the complete interaction may be dependent on either contribution or the combination of these interactions.

2.4.2.2.1 Spin-dependent interaction

In spin-dependent interaction, the WIMP interacts with the spin of the nucleus. Spin dependent interaction with axial vector couplings involves squark and Z exchanges and depends on the spin of the target nucleus. In this case, where the nucleus has an odd number of neutrons or protons, the cross-section is proportional to the spin value, J. The enhancement factor appears in equation (2.12) in this type of interaction and it is given by,

$$C_A^{SD} = \frac{8}{\pi}\left[a_p < S_p > + a_n < S_n >\right]^2 \frac{J+1}{J} \quad (2.13)$$

where a_p and a_n are the WIMP- proton and WIMP-neutron coupling strength respectively, and $< S_p >$ and $< S_n >$ are the expectation values of spin content of the proton group and neutron group respectively. J is the total angular momentum of the nucleus, for ^{19}F as a target nucleus $< S_p > = 0.44$ and $< S_n > = -0.9$ [29]. For all paired spins in the target nucleus, the spin-dependent coupling sums to zero and hence the interaction rate is dependent on the spin-content of the odd nucleon whether it is a proton or a neutron.

2.4.2.2.2 Spin- independent interaction

In spin-independent interaction, the WIMP interacts with the mass of the nucleus. Spin-independent or scalar interaction proceeds through Higgs and/or squark exchanges. In this interaction, the cross-section is proportional to the square of mass of the nucleus. The enhancement factor in equation (2.12) is given by,

$$C_A^{SI} = \frac{1}{4\pi}[Zf_p + (A - Z)f_n]^2 \quad (2.14)$$

where f_p and f_n are the WIMP-proton and WIMP-neutron coupling respectively, Z is the number of protons and A is the number of nucleons. As neutralinos are Majorana particles, it is predicted that $f_p \approx f_n$ giving $C_A^{SI} \propto A^2$. This indicates that heavy target nuclei provide a greater probability of interaction than lighter ones. Using this assumption the cross- section in the case of ^{19}F becomes,

$$\sigma_p^{SI} = \sigma_F \left(\frac{\mu_p}{\mu_F}\right)^2 \frac{1}{A^2} \quad (2.15)$$

where μ_p and μ_F are the WIMP- proton and WIMP- fluorine reduced masses respectively, and A= 19. The limits on σ_F can be transmitted into an upper bound on the WIMP-proton cross-section in the spin- independent sector with maximum sensitivity around $M_\chi = 20$ GeV/c^2 [29].

The WIMP- nucleus elastic scattering cross-section is generally dependent on the magnitude of momentum transferred to the nucleon. So the characteristic interaction length, λ, is dependent on the average momentum transfer, q(v), where v is the relative velocity of two particles. For values of M_T and $M\chi$ in the range 10 -1000 GeV/c^2 and v = 10^{-3}c, then $\lambda = 10^{-14}$–10^{-15} m, what is larger than the size of a typical nucleus. So the interaction must be with the nucleus as a whole [30, 31].

2.5 Detection techniques and direct detection experiments around the World

In order to reduce or reject unwanted background events and to allow only rare WIMP-induced signals, experimentalists have spent a lot of time and effort. Experimentalists realized that underground operation is preferred to suppress nuclear recoils from neutrons produced by cosmic ray muons. Methods of discriminating between electron and nuclear recoils were developed to reject γ and β-decay background in the target and detector component. Moreover, many direct detection search projects like PICASSO, COUPP and SIMPLE produced detectors that are insensitive to background signals from γ's and electrons.

Almost all direct-detection experiments expect to measure a small amount of energy deposited when a WIMP scatters off an atomic nucleus elastically. These experiments are designed with the requirement to be very sensitive to tiny perturbations inside their active volumes. Very sensitive electronics devices, such as piezoelectric sensors or photo sensors, are attached to the detector surface or walls to record information (sound, light, heat or vibration) about the interaction inside the detecting medium. Direct detection dark matter detectors can be grouped into four categories viz. superheated liquid detectors (detail discussions in chapter 3), scintillation detectors, cryogenic crystals detectors and noble liquid detectors. There are three main energy channels through which nuclear recoils are detected viz. ionization, scintillation, and phonon/heat.

Scintillation detectors are based on the principle that when a charged particle strikes the scintillator, its atoms are excited and as a result photons are emitted and then detected. Examples include crystal detectors such as CsI, NaI and noble liquid detectors such as Xe, Ar or Ne. Background discrimination is based on the event's light pulse decay times. Generally, it is found that nuclear recoil events produce light pulses with shorter decay times than e- or γ- ray induced events. Thus decay time analysis allows for background discrimination. Scintillation detectors experiments include: DAMA/LIBRA, NAIAD, and KIMS.

Noble liquid detectors using Xe, Ar or Ne are the most promising active volumes for large mass detectors. These detectors, containing LAr, LXe or LNe, can efficiently act as targets for WIMP detection. Since they have high density and atomic number and large target masses, these detectors provide high event rates. They have high scintillation and ionization yields due to their low ionization potentials. Scintillation and ionization are measureable and can be used to discriminate between nuclear recoils and γ - , e- backgrounds induced events. Detectors using those targets are operated by two different concepts viz. single phase detectors and double/dual phase detectors. Single phase detectors measure the scintillation signal in the liquid whereas the background reduction is achieved by pulse shape discrimination. Dual-phase detectors have a liquid that creates a scintillation signal from a nuclear recoil that is detected by photo sensors, whereas the ionization electrons from the interaction site drift towards the gas phase on top of the liquid by due to homogeneous strong applied electric field of around 1 kV/cm [32]. The electrons drift towards the top of the cylindrical detectors, where they are extracted into the gas phase above the liquid and generate a secondary light signal which is proportional to the charge. Nuclear recoils can be discriminated against γ, β and α interaction by the comparison of the relative pulse heights between primary and secondary scintillation light due to decay coincidence. Noble liquid detectors experiments include: XENON, LUX and DEAP.

Cryogenic crystal detectors operate at low temperature in the few mK range to search for dark matter particles. These detectors are designed with the primary function of detecting the phonons (lattice vibrations) produced by particle interactions using

superconductors or semiconductor thermometers. The distinct phonon signal combined with the ionization or scintillation signals provides a powerful tool for background discrimination. Cryogenic detectors with improved designs, strong background discrimination, and reduced thermal noise due to very low operating temperature are widely accepted all over the world. Cryogenic crystal detectors experiments include: CDMS/SCDMS, CRESST, and EDELWEISS.

Chapter 3

3 PICASSO

The Project in Canada to Search for Supersymmetric Objects (PICASSO) is an experiment to search for cold dark matter through the direct-detection of Weakly Interacting Massive Particles (WIMPs) via spin-dependent and spin-independent interaction with ^{19}F nuclei. PICASSO uses superheated droplet detectors to search for neutralinos based on the principles of the bubble chamber technique [33].

3.1 Detection principle

PICASSO is searching for WIMPs using a superheated liquid C_4F_{10}. The characteristics of the liquid are: boiling point -1.7 ^{o}C at 1.013 bar pressure and critical temperature 113.3 ^{o}C. The detectors contain superheated C_4F_{10} droplets in a polymerized gel matrix that provides a nearly ideal interface surrounding each droplet. The detector operation is based on the bubble chamber technique. In this technique, the detector medium is a meta-stable superheated liquid and a phase transition occurs due to energy deposited by the incoming particles (heat spikes) which may create triggers.

The response of superheated bubble detectors (SBD) to incoming particles is determined by various factors such as the particles linear energy transfer (LET), the operating temperature, the external pressure P_e applied to the detector, as well as the intrinsic properties of the active liquid. The intrinsic properties of the liquid are a) the surface tension, $\sigma(T)$, b) critical temperature T_c, c) the boiling point, T_b, and d) vapor pressure, $P_v(T)$ at a given temperature. The critical temperature is defined as the temperature above which the liquid phase can no longer exist; the boiling temperature is defined as the temperature above which a fluid becomes either a superheated liquid or vapor.

It was previously mentioned that SBDs are based on the Seitz's theory of bubble chamber operation [33]. According to this model, the superheated liquid allows phase transition due to the heat spikes produced by the energy deposited along the track of travelling particles.

It is noted that the liquid will be thermodynamically stable at a given temperature within the range between T_b and T_c if the external pressure is greater than the vapor pressure. In this case, the detector will be insensitive to incoming particles. If the external pressure is decreased to below the vapor pressure, then the droplets become superheated with a tendency to undergo a phase transition from liquid to gas. The degree of superheat depends on the difference between the vapor pressure and the external pressure. In this condition, superheated droplets will turn into a vapor bubble if the droplet gets enough extra energy by the heat spikes due to the energy deposited by an incoming particle. However, if it is left undisturbed or if no extra energy is provided, the liquid remains in its meta-stable state as it must overcome a potential barrier to make the transition from the liquid to the gas phase. This potential barrier is given by Gibb's equation [34],

$$E_c = \frac{16\pi}{3}\frac{\sigma^3(T)}{(P_v(T)-P_e)^2} \tag{3.1}$$

where $P_v(T)$ is the temperature dependent vapor pressure, P_e is the external pressure and $\sigma(T)$ is the surface tension at the liquid-vapor interface at temperature T and is given by,

$$\sigma(T) = \frac{\sigma_0(T_c-T)}{(T_c-T_{0)}} \tag{3.2}$$

where σ_0 is the surface tension at a reference temperature, usually the boiling temperature, T_b.

If the deposited energy E_{dep} exceeds a threshold energy E_{th} at a given temperature, a bubble is formed within a distance $L_c \approx aR_c$, R_c is the critical radius and is given by [35],

$$R_c = \frac{2\sigma(T)}{(P_v(T)-P_e)} \tag{3.3}$$

and a is a constant whose values vary from 2 to 18 [35, 36, 37]. The linear energy transfer (LET) in the liquid is defined as $\frac{dE}{dx}$ and the energy deposited by the particle on its track along L_c is given by,

$$E_{dep} \approx \frac{dE}{dx} \ . L_c \tag{3.4}$$

Hence the condition necessary to trigger a liquid to vapor transition becomes $E_{dep} \geq E_{th}$.

However, it should be noted that the deposited energy given by equation (3.4) is not the total deposited energy that will trigger a liquid to vapor-phase. A part of this energy is transformed into heat [38]. So the actual threshold energy for radiation or nuclear recoil is related to critical energy E_c by an efficiency factor $\eta = \frac{E_c}{E_{th}}$ where η lies between 2−6% [35, 38].

If the deposited energy exceeds the threshold energy E_{th}, there is a greater chance of a possible explosion from liquid to vapor phase. This phase transition is explosive in nature and is accompanied by an acoustic signal in the audible to ultra-sonic frequency range, which can be registered by a piezoelectric transducer attached to the walls of the detector. The probability P that an energy deposition larger than the threshold energy will create a nucleation site is given by,

$$\mathrm{P}\left[\mathrm{E_{dep}}\,,\mathrm{E_{th}(T)}\right] = 1 - \exp\left[\alpha\left(1 - \frac{\mathrm{E_{dep}}}{\mathrm{E_{th}(T)}}\right)\right] \tag{3.5}$$

where α is a parameter determined experimentally and describes the observed steepness of the threshold and reflects the statistical nature of the process [39].

Chlorofluorocarbons such as C_3F_8, C_4F_{10}, CF_3Br, CCl_2F_2 and their combinations are superheated at room temperature and ambient pressure in the absence of heterogeneous nucleation. So they are suitable and attractive for particle detection experiments. Almost all detectors used in direct dark matter detection experiments using SBDs (such as PICASSO, COUPP, and SIMPLE) use these liquids. d'Errico introduced a

new reduced superheated variable [40] 's' to compare the response of different liquids. The reduced superheat variable depends on T, T_B and T_C and is given by,

$$s = \frac{T - T_B}{T_C - T_B} \tag{3.6}$$

The value of s lies between 0 and 1. For any gas, for $P_e = P_v$ at $T = T_B$, s = 0 and at $T = T_C$, s = 1. s = 0 and s = 1 represent the lower limit and upper limit of the superheated state respectively.

Droplet detectors are threshold counters in which individual superheated droplets act as independent bubble chamber detectors. The operating temperature and the pressure applied to the liquid determine this threshold. At higher temperatures the energy threshold for nuclear recoil is lower. The ^{19}F threshold energy as a function of temperature to produce nuclear recoil by different incoming particles (alpha, gamma, and WIMPs) is shown in figure 3.1.

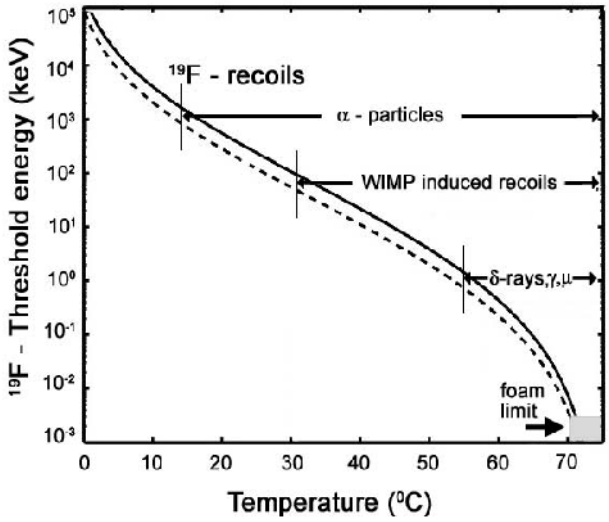

Figure 3.1: Threshold energy for ^{19}F recoils as a function of temperature at a pressure of 1.23 bars. The continuous line indicates 80% and dashed line indicates 50% recoil detection efficiency. The detectors become sensitive to α- particle above 15 ^{o}C, WIMP-induced recoils become detectable above 30 ^{o}C, and γ-rays and MIP become detectable above 55 ^{o}C [35].

This curve shows the relationship between the ^{19}F threshold energy and the temperature over which the recoil is produced by these particles. This is very useful to discriminate background particles from the background radiation such as minimally ionizing particles and gamma rays.

The normalized detector response (count rate) when loaded with C_4F_{10} droplets of 200 μm diameter as a function of temperature for different types of particles, including the expected response to WIMPs of mass 50 GeV/c^2, is shown in figure 3.2. The detector's response to WIMPs is obtained by simulation whereas the known background such as alpha particles, neutrons and gamma rays are obtained from the measurements.

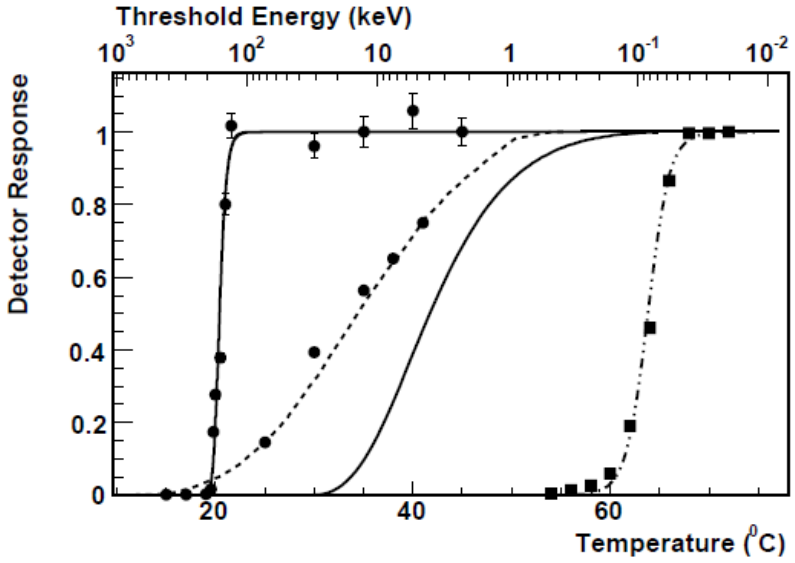

Figure 3.2: Normalized detector response to different types of particles as a function of temperature for detector loaded with C_4F_{10} of droplets of 200 μm diameter. From left to right: 5.6 MeV alpha-particles from a detector spiked with ^{226}Ra, neutrons from an AmBe source, expected response to 50 GeV/c^2 WIMPs and gamma rays [39].

3.2 Detector fabrication and installation

The latest generation PICASSO detector is shown in figure 3.3. It consists of cylindrical modules of 14 cm diameter, 1.4 cm wall thickness, and 40 cm height. The containers are fabricated from acrylic and closed from top and bottom by stainless lids sealed with

polyurethane O-rings. Each detector is filled with 4.5 L of polymerized gel loaded with approximately 80 g of active mass of C_4F_{10}. The active C_4F_{10} is in the form of droplets with size ranging between 200−500 μm, on average 242.30 ± 159.20 μm (95% C.L.) (based on the measurement at Laurentian University). Initially PICASSO used small droplets sized around 50 μm. It is believed that the background particles such as alpha-particles may not diffuse properly and cannot create multiple nucleation sites if the droplet size is small. Therefore, the current generation of PICASSO detectors uses larger size droplets.

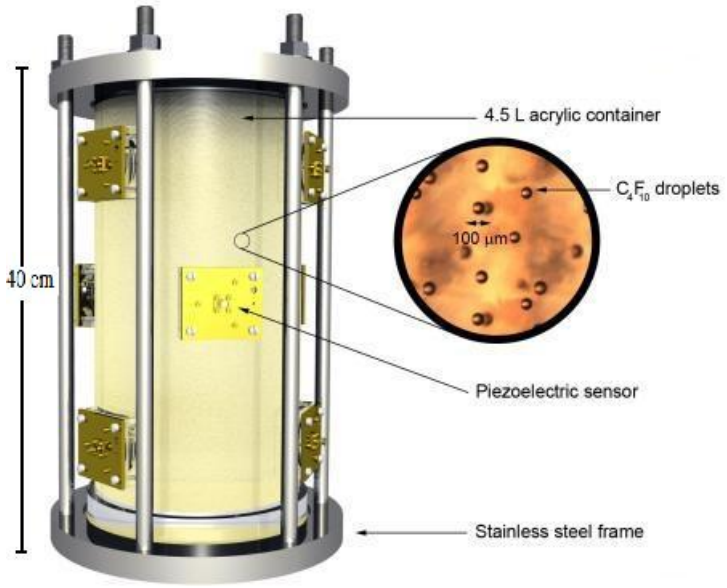

Figure 3.3: Current generation of PICASSO detector. It is a 4.5 L module with approximately 80 g of active mass of C_4F_{10}. Droplets are suspended in an elastic polymer. Signals are recorded by nine piezoelectric sensors [41].

The detailed investigation of the droplets size distribution in the detectors and measurements will be discussed in Chapter 5. Mineral oil thickness of 3−4 cm on top of the gel is used to prevent the gel from drying out as well as to remove air, hence allowing the detector to be pressurized. Nine piezoelectric transducers are attached on the outside walls of the acrylic cylinders at different locations: top, middle, and bottom in order to register the acoustic signals due to the phase transition and to maximize signal measurement efficiency and allow localization of events.

The detectors are fabricated in clean rooms at the Université de Montréal and Queens University by the Collaboration. In the initial phase, PICASSO used salty detectors: CsCl salt was used in the gel to match the density of the final gel solution with that of the C_4F_{10} droplets so that they were suspended during the polymerization process. But this salt contained radioactive contamination with alpha-emitters, such as U, Th, and their decay daughters, leading to large background rates. Even after purification of CsCl, it was still contaminated and contributed a significant internal background from alpha - particles. The latest generations of PICASSO detectors are completely salt-less to remove this background. This new technique of gel fabrication was developed by Xiongxin Dai [42, 43]. Presently, PICASSO operates only salt-less detectors.

These detectors are divided into groups of four and placed inside eight thermally-insulated boxes, called temperature pressure control system (TPCS) as shown in figure 3.4, of external dimensions 56 × 65 × 65 cm^3. The entire installation is surrounded by water tanks that absorb neutrons from the surrounding rocks and concrete or those produced by nuclear reaction. The figure 3.5 shows the entire installation of the detectors with neutron shielding.

Figure 3.4: The inner parts of a TPCS with four detectors.

The operating temperature of the detectors is varied from 20 ^oC to 50 ^oC, with a precision of ± 0.1 ^oC. The different types of runs, consisting of calibration or WIMP runs, are conducted at ambient pressure. A typical WIMP run lasts 40 hrs whereas calibration

runs last 40−90 minutes. After completion of each cycle, the detectors are recompressed for about 11 hrs at 6.2 bar pressure to return the C_4F_{10} bubbles formed during the run into liquid droplets.

Figure 3.5: Installation of the PICASSO experiment at SNOLAB.

3.3 Response of background radiation and discrimination

To detect new or unknown particles, it is necessary to check the response of the detectors to all known background. It is also desirable to learn all information and nature of the known particles to distinguish them from the discovered particles. This is one of the reasons why all direct detection dark matter search experiments such as PICASSO, COUPP, and SIMPLE began their experiments with calibration runs using known sources of neutron, alpha and gamma-ray emitters.

3.3.1 Neutron Response

To understand the response of PICASSO detectors to neutralino-induced nuclear recoils, it is necessary to study the interaction of low energy neutrons ($E_n \leq 500\ keV$) with the superheated droplets (C_4F_{10}). This interaction leads to recoils of ^{19}F and ^{12}C nuclei that trigger the liquid to vapor phase transition. The recoil energy of nuclei (^{19}F and ^{12}C

nuclei) is given by equation (2.10). The recoil energy is maximum when $\theta = 180°$. A fraction of the energy of the incident neutron is transmitted into nuclei. For a detailed explanation, please see ref. [35, 44]. The ranges for ^{19}F and ^{12}C nuclei depend on maximum recoil energy of nuclei and on their specific energy losses, dE/dx. The nuclear recoil energy is determined by the ^{19}F and ^{12}C recoil angular distribution. It is noted that not all recoil energy depositions are detectable as SBD is a device working on threshold energy and hence there exists a threshold recoil energy below which no phase transition occurs. It was mentioned in section 3.1 that the threshold nuclear recoil energy depends on the operating temperature and pressure.

The neutron threshold recoil energies required for phase transition are determined by exposing a 10 mL test detector loaded with C_4F_{10} droplets to a mono-energetic beam of neutrons at different temperatures and pressures. These mono-energetic neutrons were produced by the nuclear reaction, ^{7}Li (p, n) ^{7}Be, with mono-energetic protons from the Tandem Van de Graff facility at the Université de Montréal. The count rate, as a function of temperature and pressure for 200 keV neutrons at different operating pressures, is shown in figure 3.6.

The study of the interaction of neutrons with the SBD detector is very important as SBD's response to neutrons is similar to WIMPs'. Hence, neutrons are the main background, making necessary to shield the SBD from neutrons in order to detect WIMPs. The PICASSO detectors are shielded from neutrons due to cosmic rays by being installed 2 km underground and by using thick water tanks surrounding the entire set up; its shielding efficiency is about 98% [45].

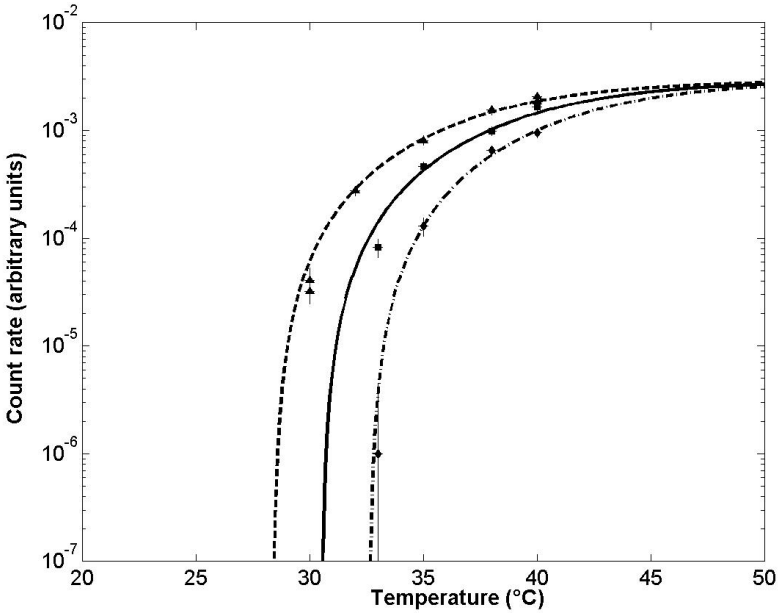

Figure 3.6: The response of a SBD loaded with C_4F_{10} response to 200 keV neutrons as a function of temperature at three different pressures (from left to right: 1.01, 1.36, 1.7 bar) [35].

3.3.2 Alpha particle Response

The primary source of background radiation comes from inside the detector itself in the form of alpha-particles. Alpha-particles produced in the Freon and in the surrounding gel matrix are the dominant intrinsic background for PICASSO. Alpha-particles emitted by U and Th contaminants in the heavy salt CsCl that was used in the first stage/generation of the PICASSO detector was the main source of background radiation. It was very important to improve the purification process of the gel component to reduce the alpha-particles background. Even after purification of the gel, the detector response to α-particles has to be known with high precision. Therefore, it is necessary to know the response of PICASSO detector to α-particles.

The alpha-response was studied by spiking the gel of a detector with alpha-emitting sources of known activities. The detectors were placed in a thermally and acoustically insulated container, the TPCS, temperature controlled with a precision of

0.1^{o}C [35]. The alpha-response, defined as counts per emitted alpha-particle per gram of Freon over the range of temperature, was measured. The series of measurements was performed using different types of detectors with different radioactive sources ^{232}U, ^{241}Am, ^{238}U, with different known activities.

The α-responses of the two (C_4F_{10}) detectors spiked with ^{241}Am and ^{238}U as a function of temperature is shown in figure 3.7, along with the results of simulations [35]. It is observed that the maximum value of the response of a detector spiked with ^{241}Am is greater than for the detector spiked with ^{238}U.

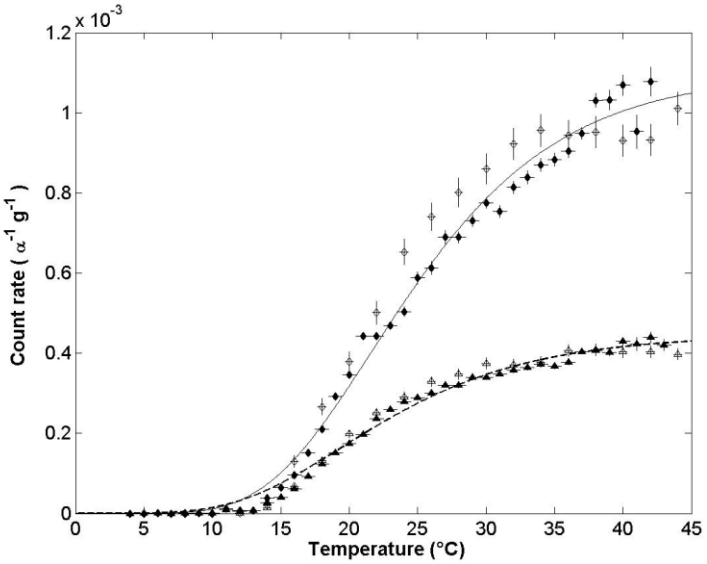

Figure 3.7: The normalized α-response of two detectors as a function of temperature spiked with ^{241}Am (solid diamond) and ^{238}U (solid triangle) along with the simulation results for both ^{241}Am (open diamond) and ^{238}U (open triangle) [35].

3.3.3 Gamma Response

PICASSO detectors are insensitive to gamma-rays and to minimum ionizing particles (MIPs) such as cosmic ray muons, and beta-rays at the operating temperature, 20−50 ^{o}C. They are detectable and observed in PICASSO detectors only above 55 ^{o}C. As PICASSO detectors operate below 50 ^{o}C, it is not necessary to shield the detectors from

such types of radiation. This is one of the main advantages of PICASSO detectors over detectors used by other direct detection of dark matter search experiments.

The response of the PICASSO detectors to gamma rays was studied using a ^{22}Na source having an activity of 0.7 μCi. Two 10 ml detectors were used to study gamma-ray response. The gamma-ray detection sensitivity was measured from 49.5 ^{o}C to 70.7 ^{o}C. A detailed explanation of the gamma rays detection sensitivity as a function of temperature can be found in [35].

3.4 PICASSO at SNOLAB

Rare event experiments such as double beta-decay, study of weak interactions from cosmic neutrinos, direct detection of dark matter candidates and nuclear astrophysics studies require low-background environments that can only be achieved in a shielded and clean underground environment. So, underground laboratories with low radioactive background and clean environments are the ideal places for direct detection of dark matter. SNOLAB, located at 2 km underground in the Vale Creighton mine, near Sudbury, Ontario, is a world-class international facility for deep underground science. The depth of two kilometers is adequate to protect the detectors from cosmic rays and its class 2000 clean room environment is another valuable feature for the dark matter search experiments.

There are mainly two types of neutrons that affect dark matter detectors. They are fast neutrons, produced by muons traversing the detector itself, and neutrons created in the external rock e.g. through α-n reactions. The former depends on the depth and composition of an underground site in which the cosmic-ray muon flux decreases by increasing the depth of the underground site. Measurements of cosmic-ray muon flux and muon-induced fast neutron flux as a function of depth for specific existing underground laboratories around the world are shown in figure 3.8. The measured neutron flux was derived utilizing the FLUKA simulation with the corrected neutron multiplicity and the measured muon flux and distributions [46].

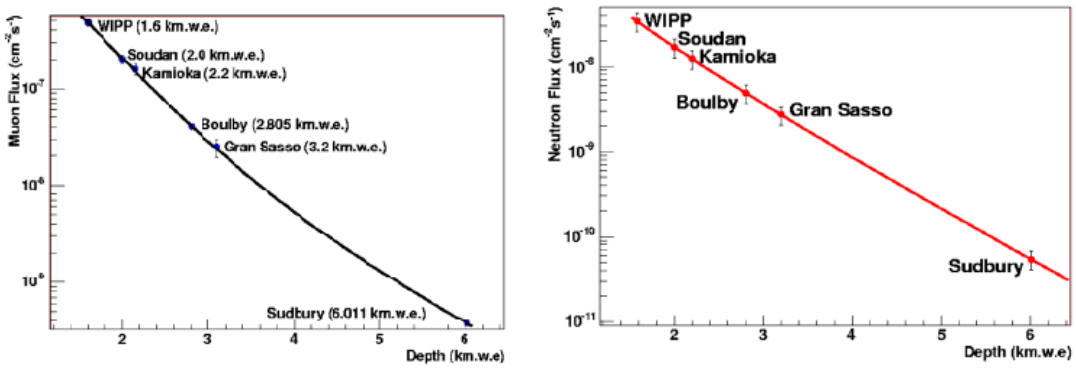

Figure 3.8: The cosmic-ray muon flux (left) and the muon-induced fast neutron flux (right) as a function of depth, in kilometers water equivalent, for existing underground laboratories around the world [46].

It is seen from the muon-, and neutron-flux plots that SNOLAB in Sudbury has the lowest cosmic-ray flux and the lowest neutron flux; therefore, the detectors operated at the SNOLAB have the lowest background event rate compared to all other underground laboratories around the world.

3.5 PICASSO results

PICASSO latest results, published in February 2012, are based on the data taken from 2008 to 2011 using a subset of 10 detectors with a total target mass of 0.77 kg of ^{19}F and an exposure of 114 kg days. The sensitivity to interactions from WIMPs with masses below 10 $GeVc^{-2}$ was increased by reducing background to allow a recoil energy threshold of 1.7 keV. The combination of light target nucleus ^{19}F with the low detection threshold of 1.7 keV for recoil nuclei renders PICASSO particularly sensitive to low mass regions of the spin independent sector. The main improvements with respect to previous results published in 2009, can be explained as follows: Alpha background was reduced by a factor of eight, discrimination of non-particle induced events was extended to the lower threshold recoil energy, and the analysis was extended from 2 to 10 detectors.

In order to search for a dark matter signal, the count rates were measured as a function of threshold energy and compared to predicted values for interactions of WIMPs in the galactic halo with ^{19}F nuclei plus constant alpha background in the detectors. The calculation is based on the formalism described in [28]; its detailed explanation can be found in section 2.4.2. The count rate or event was normalized with respect to the active mass (^{19}F) and data was taken for all temperatures. No dark matter signal was detected. For the spin dependent sector, where the scattering of dark matter on ^{19}F is dominated by interactions with protons, the analysis yielded exclusion limits of $\sigma_p^{SD} = 0.32\, pb$ (90% C.L) for a WIMP mass of 20 GeVc^{-2} [29]. The resulting exclusion curves for the WIMP cross-section on protons as a function of WIMP mass are shown in figure 3.9 together with other published results in the spin dependent sector.

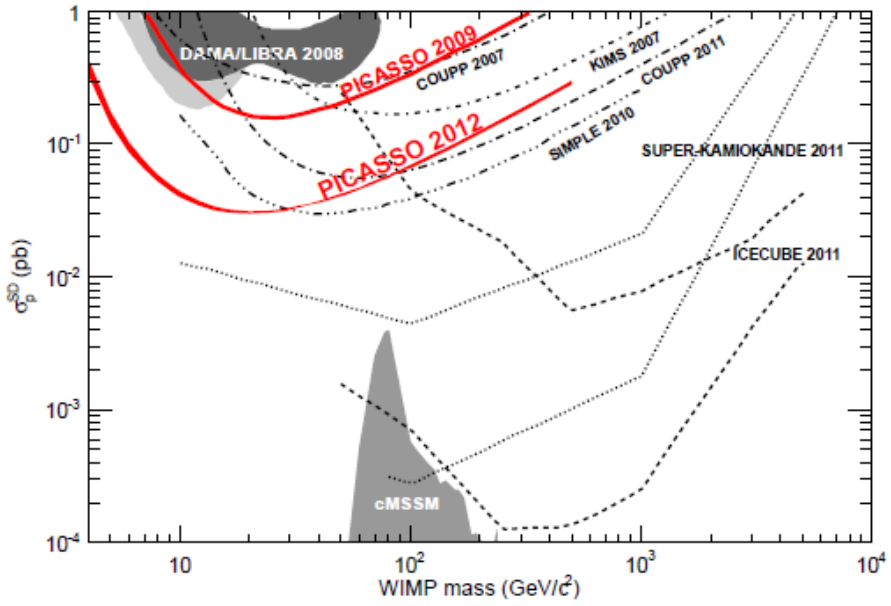

Figure 3.9: Upper limits at 90% C.L. on spin dependent WIMP-proton interactions. PICASSO limits are shown as full lines [29].

Chapter 4

4 Alpha-neutron discrimination

This experiment was designed to discriminate alpha and neutron induced signals by analyzing both the image and the acoustic signal of each event due to clear phase transition. Here clear phase transition means independent event, not in a cluster. If the event happened in a cluster, this event would not be a good event. At first, a good event was confirmed by carefully observing the live event image along with the signal. The good events are defined as the events where the signal can be correlated with an image of a bubble. It was focused on taking images of each event with an observed phase transition. Taking the image of each event not only gives a clear image of the event but also confirms it is a real particle-induced event, and making it easy to separate the events produced due to the ambient noise in the laboratory. Consequently, it is also useful to analyze and confirm the real particles induced events due to different background particles like alpha, neutron, and gamma and to disregard the unnecessary noise and noisy events.

4.1 Experimental methods

4.1.1 Sound insulation of experimental box

Initially, false signals were encountered from the acoustic noise registered by the piezoelectric sensor due to interference from human activities in the laboratory, vibrations from the fan, air-flow, electric noise and others. In some runs, there were 1000 events registered within 12 hrs of which only 10-15 events were deemed good events after observation and analyses of each event's image frame. Finally, the sources of noise were found which allowed for minimization and in some cases completely suppression. To remove the acoustic noise produced in the lab, the experimental box was isolated from inside and outside by a special type of sound insulator made from melamine foam. The fan of the Peltier device (used for heating), attached at the wall of the box, was another

main source of noise; to remove this noise, a chimney-like structure of metallic tubing was used and kept the fan about 40 cm from the box wall. All these constructions helped to reduce the noise level from 400 mV to 50 mV. The complete sound isolated experimental box is shown in figure 4.1 below. The remaining noise due to the electric plug and grounding could not be removed easily and induces a negligible error.

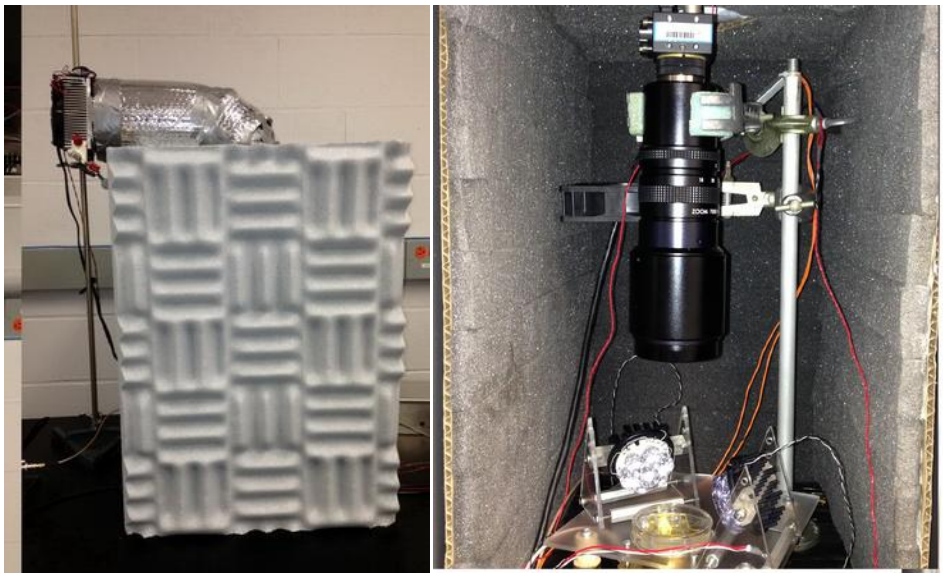

Figure 4.1: Outside and inside sound and heat insulated experimental box.

4.1.2 Trigger board

It has been already mentioned that two devices were used to take the data: the DAQ system and the camera. Initially, the two devices worked independently. Time stamp in the data log files from both devices were used to match events in the two systems. It was a very slow, time consuming, and imprecise method. In order to develop a very precise method to synchronize the camera with the DAQ, a trigger board was developed at Laurentian University to synchronize both devices. The trigger board was designed and built by Dr. Ruslan Podviyanuk. The basic information and function of the main parts of trigger board is explained briefly here.

The block diagram of the trigger unit is shown in figure 4.2. The operational amplifier (label 1 in figure) with gain one, transmits the signal from the preamplifier to

the comparator (label 2 in figure) without any changes of amplitude. The operational amplifier is used to match the impedances of the preamplifier and the trigger unit and to prevent damage to the trigger unit input. The main function of the comparator is to convert analog signals to digital signals. The digital signal from the comparator will be created if the input analog signal is greater than the threshold; this digital signal is TTL (Transistor-Transistor Logic). The signal from the comparator can trigger both the camera and the DAQ. The comparator threshold was chosen to be positive (starting from 20 mV, but adjustable) and all amplitudes of signal higher than threshold will create trigger pulses (see Figure 4.3).

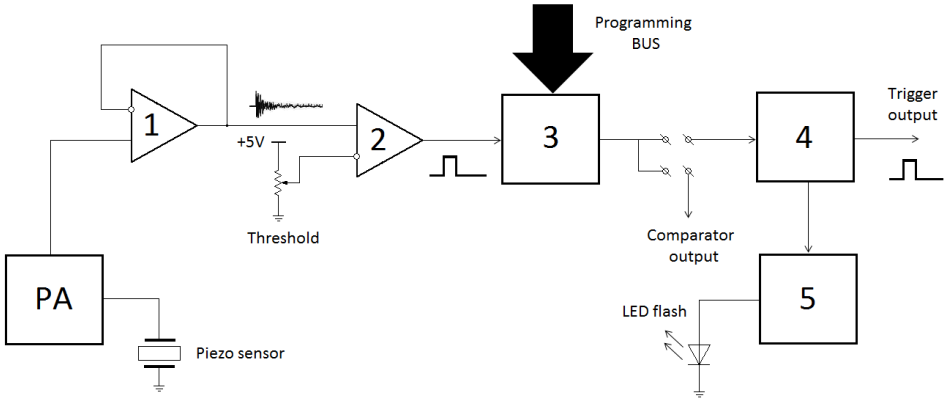

Figure 4.2: Block diagram of trigger unit showing main parts: Preamplifier (PA), Operational amplifier (1), comparator (2), microcontroller (3), mono-stable multi-vibrator (4) and light activator (5). Courtesy of Dr. Ruslan Podviyanuk.

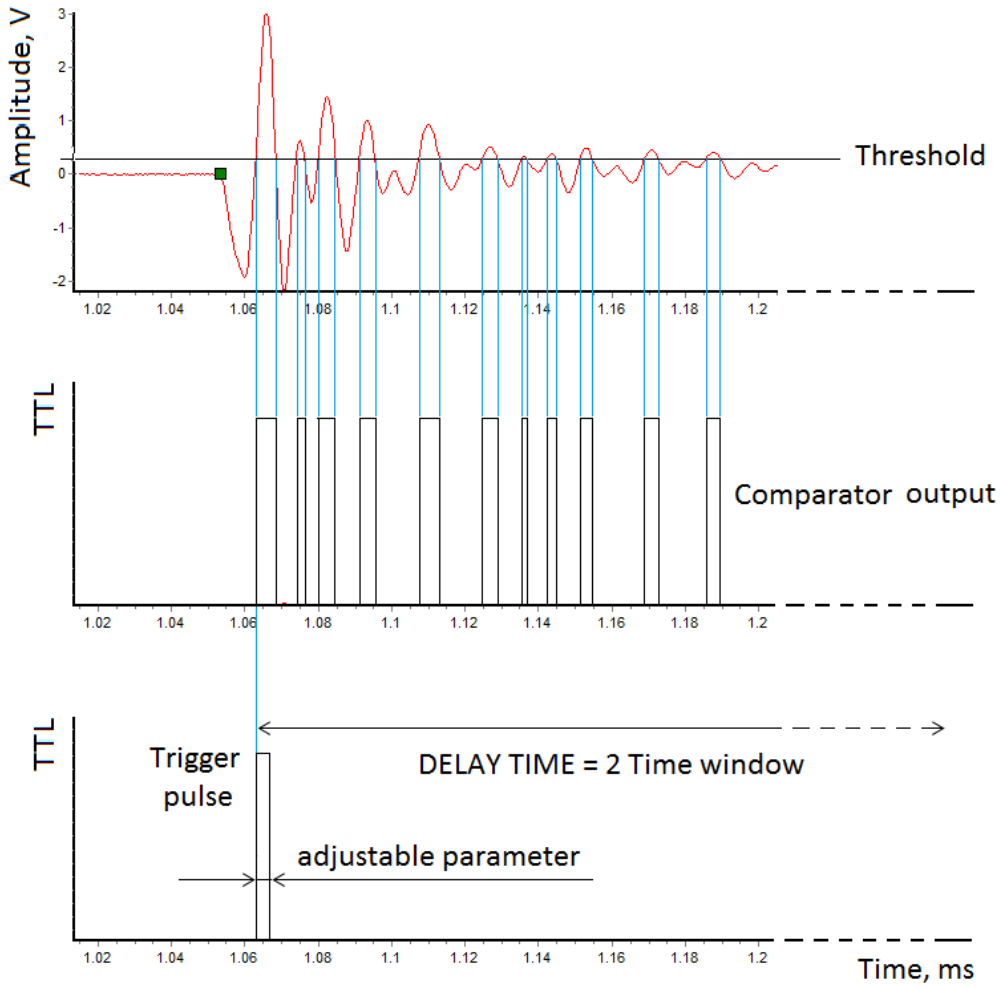

Figure 4.3: TTL triggering output pulse from comparator, microcontroller algorithm.

The time window of the DAQ signal is adjustable. In this measurement, the time window is 10 ms. In this time window, the DAQ starts to digitize a signal from the part of the sine wave greater than threshold and stops at the end of the time window. But in case of the camera does not have this situation. The time window of the camera cannot be adjusted. So, if the camera is fast it can take more pictures than the events registered by DAQ due to many triggering signals from the comparator. To solve this problem, the trigger board contained a microcontroller (label 3 in figure) to make a lock-out time equal to $2 \times \text{time window} = 20$ ms. As a result, instead of many trigger signals from the comparator only one trigger signal with adjustable pulse duration 2–20 µs which is good for both camera and DAQ. The duration of the trigger pulse is adjusted by a mono-stable

multi-vibrator (label 4 in figure). Beside these main parts, the trigger unit has other parts such as a transistor-based (label 5 in figure) light activator.

4.1.3 Experimental arrangement and set up

The experiment consisted of two phases:

Phase I: The camera and the DAQ system working independently

In order to measure the acoustic signal produced due to phase transition of the Freon droplets (i.e. droplet burst events) and the corresponding bubble size, an experiment was designed. A digital ("Infinity") camera with resolution 640×480 focused on a sample of gel is placed on a petri dish with the bottom part replaced by an aluminum plate of thickness about 1 mm. Physical Acoustics (R15 TOPCON, or Micro 200 HF) or customized PZB REGULAR PICASSO piezoelectric-sensors were directly attached to this aluminum plate one at a time to register the waveform of events. Three different piezoelectric sensors were used in different runs to find a suitable one for this experiment and finally chose the PZB REGULAR PICASSO. The sample of gel was kept on a petri dish filled with mineral oil. The mineral oil was used for two purposes: to prevent the sample of gel from drying and to remove the air bubbles. The piezoelectric sensor is connected via SMA-BNC cable to a Mitras amplifier with linear gain as shown in figure 4.4. An Alazar DSO DAQ system was used to digitize the signal. The parameters used for signal digitizing were as follows: sampling rate 2 MHz, pre-trigger information 1ms, and time window 10 ms (resulting in a signal duration of 9 ms).

At First, the digitized signals were saved in the Alazar DSO folder with a corresponding time stamp. All waveforms were saved in a single folder with detailed information. Typical computer software was developed to convert each waveform into the standard format used at Laurentian University (event-by-event ASCII file format). The infinity camera was connected to a PC via USB cable and was operated using the software HandyAVI, which captures and records images only when motion is detected i.e. when the droplet turns into bubble. Initially, the images were saved as an AVI movie

file that had a corresponding log file giving the accurate time at which each frame was captured.

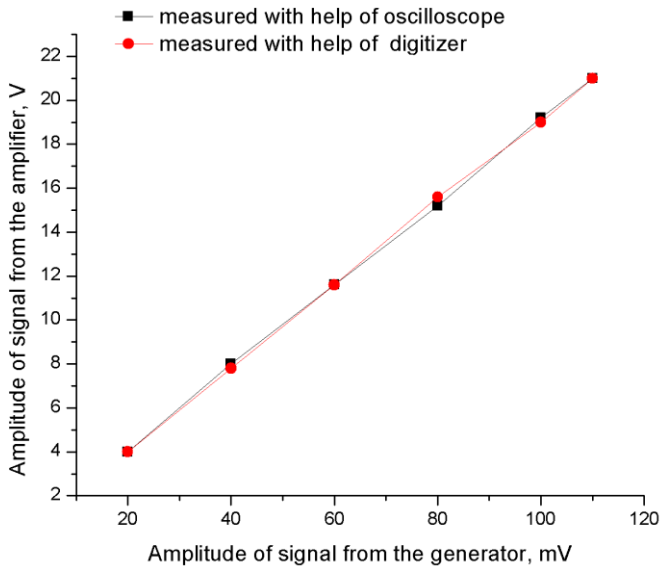

Figure 4.4: The linear gain of Mitrass amplifier set with gain 55 dB (40 dB preamp and 15 dB amp). Signals were created from a waveform generator which was connected directly to the preamplifier input.

To identify good events, the time stamp of each event file were compared and matched manually. It was very difficult and time consuming. So it realized the necessity of computer programming to compare and match the time stamp of both camera files and DAQ files. The computer programming developed at Laurentian University was used which was reliable and easy to compare the events from AVI log file and the DAQ file, which is shown in figure 4.5 below This program was used to find the good events by matching the time stamp of the AVI log file and the DAQ file. The coincidence time stamp is saved in a separate text file. The blue bars represent the coincidence event i.e. good event in figure 4.5.

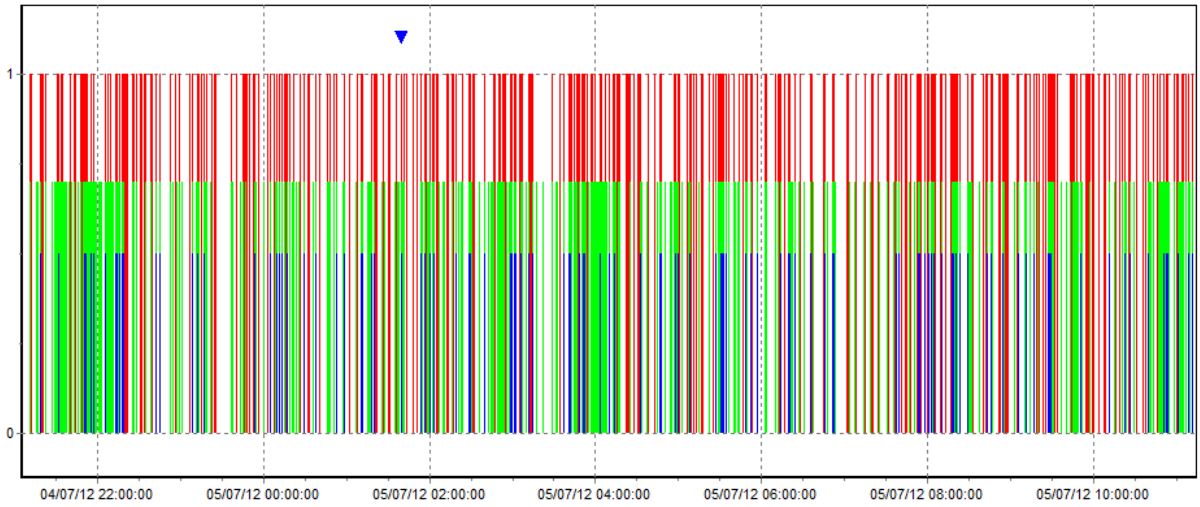

Figure 4.5: The time of coincidences between signals and images. Red bars represent signal, green bars represent image frames and blue bars represent coincidence of both.

Two strong LED light sources were put in each side of the petri dish where the gel sample was kept. The entire apparatus was contained within a sound-insulated temperature-controlled box. The temperature was controlled by a Peltier-based heating and cooling unit (TE Technology) operated by a temperature controller board connected to PC via serial cable. The block diagram of the experimental apparatus is shown in figure 4.6.

^{241}Am and ^{222}Rn were used as alpha sources. The gel samples were spiked with ^{241}Am liquid with an activity of ~2 Bq/ml and ^{222}Rn with an activity of ~10 Bq/gel sample for alpha runs and ^{252}Cf, with an activity of 728.93 Bq and inducing a count rate of ~ 82 neutrons per second was placed close to the gel sample, was used as a neutron source in neutron runs. The neutron source was put very close to the petri dish. The data were taken at different temperatures viz. 25 ^{o}C to 45 ^{o}C.

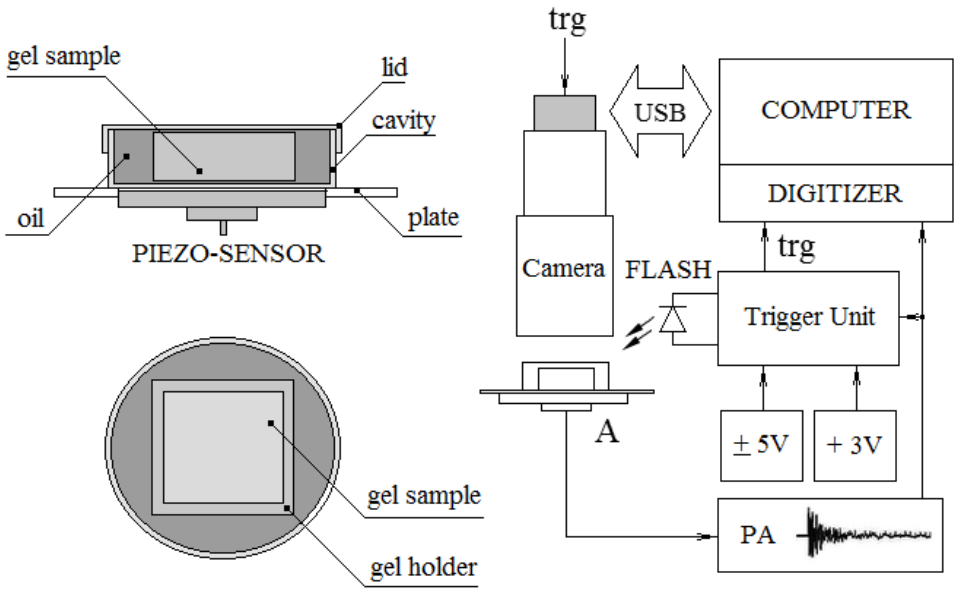

Figure 4.6: Block diagram of the experiment to measure the droplet size, bubble diameter and the signal produced due to phase transition.

Phase II: synchronization of camera and DAQ system

It was already mentioned in previous section that the data was taken using two main devices working independently. It realized that it would be best if the camera and the DAQ could synchronize. To achieve this synchronization, a trigger board was used. The block diagrams of trigger board with TTL triggering output are shown in figures 4.2 and 4.3 respectively. The experiment was based on the principle that the events due to phase transitions (i.e. droplets bursting) provide triggers to both the camera and DAQ at the same time and hence everything is recorded on camera and DAQ at the same time. This helps the waveform and its corresponding event image frame to be saved on their separate file folder with the same time stamp. Initially, this trigger board was tried to work to the Infinity camera and the DAQ using quite a different principle. When a phase transition took place, it triggered a flash of light that provides enough light for the acquired image to have a better contrast to capture a picture of the event. Unfortunately, the event image frames were not sharp and could not be analyzed. To get visually clear

pictures of event, the DMK the Imaging Source camera was chosen. This camera was synchronized through the trigger board with the DAQ system. In this phase, a holder was also developed. Actually, this construction was built like a mini PICASSO detector with a small gel sample, with holder dipped in a mineral oil. The way of data taking and all other devices and electronics were the same as explained in a previous section, phase I. The design of the experiment to measure the droplet and its corresponding bubble and also the signal produced due to phase transition, is the same as in figure 4.6, explained in phase I, except by the camera, in which the Infinity camera was replaced by DMK the Imaging Source.

4.1.4 Run details

Many runs were carried out using different sources of radiation at various temperatures viz. 25−45 ^{o}C. Tables 4.1-4.4 give the detailed list of runs that were used in data analysis with detailed information about the run types, temperature, pre-amplifier gain, run duration and total numbers of events etc. It has already been described in previous sections how to select good events with the help of the image frames. For good events, there is a correlation between the image and the waveform. Moreover, for precise measurements, only the clear independent event was considered as a good event. The events which occurred in a cluster were disregarded during data analysis due to the difficulties they posed. Most of the events were due to the presence of acoustic noise due to human activities in the lab, although the experimental box was isolated by a sound insulator. Moreover, the oil drops and the air bubbles are themselves sources of noise. If the run duration is too long or after many events, the bubble will burst and disappear resulting in acoustic signals that are unwanted events. The final confirmation of good events is made by utilizing the live event image frames. Also, to know the background radiation count and check for contamination, backgrounds runs were conducted before the neutron runs.

The alpha runs were accumulated by using two different kinds of alpha-spiked gel samples. Many computer simulations [47] suggested that it is best to locate the alpha-

emitter inside the droplets if possible. It is believed that radon diffuses into the droplets well and is therefore good for alpha runs. ^{241}Am may not diffuse inside the droplet so may not be as good for alpha runs. Unfortunately, only one option in ^{241}Am was possible to accumulate runs. A computer program, named the run maker, was developed to combine runs into a new single run. Using this program, all good events from many runs (similar in all aspects such as temperature, gain, and trigger threshold) were combined to make a single run and get good statistics.

Table 4.1: Runs at temperature 45 ^{o}C used in data analysis

Run number	Run type	Pre-amp gain, dB	Total number of events	Number of good events	Run duration (hr)
121119A045atm1bg 002	Background	55		2	19
121128A045atm1Sn102	Neutron (^{252}Cf)	55	32	7	17.13
121129A045atm1Sn103	Neutron (^{252}Cf)	55	51	13	30.66
121130A045atm1Sn104	Neutron (^{252}Cf)	55	44	17	24.16
121201A045atm1Sn105	Neutron (^{252}Cf)	55	75	31	32.78
121203A045atm1Sn106	Neutron (^{252}Cf)	55	65	22	47.23
121205A045atm1Sn107	Neutron (^{252}Cf)	55	43	12	21.26
121206A045atm1Sn108	Neutron (^{252}Cf)	55	53	15	23
121207A045atm1Sa109	Alpha spiked (^{241}Am)	55	136	16	20.38
121208A045atm1Sa110	Alpha spiked (^{241}Am)	55	123	29	21.28
121209A045atm1Sa111	Alpha spiked (^{241}Am)	55	63	20	13.8
121210A045atm1Sa112	Alpha spiked (^{241}Am)	55	105	31	22.21
121211A045atm1Sa113	Alpha spiked (^{241}Am)	55	69	19	23.83
121212A045atm1Sa114	Alpha spiked (^{241}Am)	55	62	22	20.8
121213A045atm1Sa115	Alpha spiked (^{241}Am)	55	53	14	25.26
121214A045atm1Sa116	Alpha spiked (^{241}Am)	55	107	29	27.21
121215A045atm1Sa117	Alpha spiked (^{241}Am)	55	70	17	63.6

Table 4.2: Runs at temperature 40 ^{o}C used in data analysis

Run number	Run type	Pre-amp gain, dB	Total number of events	Number of good events	Run duration (hr)
130605A040atm1bg 005	Background	55	483	5	96.58
130610A040atm1Sn159*	Neutron (^{252}Cf)	55	443	44	43.81
130612A040atm1Sn160	Neutron (^{252}Cf)	55	209	26	25.91
130613A040atm1Sn161	Neutron (^{252}Cf)	55	221	32	24.28
130614A040atm1Sn162	Neutron (^{252}Cf)	55	470	40	69.06
130617A040atm1Sn163	Neutron (^{252}Cf)	55	144	19	23.65
130619A040atm1Sn164	Neutron (^{252}Cf)	55	144	13	23.66
130625A040atm1Sa165	Alpha spiked (^{241}Am)	55	366	19	17.75
130626A040atm1Sa166	Alpha spiked (^{241}Am)	55	454	18	23.33
130627A040atm1Sa167	Alpha spiked (^{241}Am)	55	274	28	27.71
130628A040atm1Sa168	Alpha spiked (^{241}Am)	55	283	18	26.68
130629A040atm1Sa169	Alpha spiked (^{241}Am)	55	225	13	24.86
130630A040atm1Sa170	Alpha spiked (^{241}Am)	55	212	17	39.75
130702A040atm1Sa171	Alpha spiked (^{241}Am)	55	206	28	27.26
130703A040atm1Sa172	Alpha spiked (^{241}Am)	55	376	28	43.86

*Remarks: In 130610A040atm1Sn159, 130610 means year/month/day, A means first run in a day, 040 means temperature in ^{o}C, atm1 means atmospheric pressure and Sn means neutron run.

Table 4.3: Runs at temperature 35 ^{o}C used in data analysis

Run number	Run type	Pre-amp gain, dB	Total number of events	Number of good events	Run duration (hr)
130824A035atm1bg007	Background	55	353	7	258.63
130405A035atm1Sn151	Neutron (^{252}Cf)	55	112	18	31.73
130406A035atm1Sn152	Neutron (^{252}Cf)	55	197	24	38.8
130410A035atm1Sn154	Neutron (^{252}Cf)	55	162	20	23.5
130411A035atm1Sn155	Neutron (^{252}Cf)	55	132	24	25.41
130412A035atm1Sn156	Neutron (^{252}Cf)	55	307	37	51.86
130303A035atm1Sa137	Alpha spiked (^{241}Am)	55	54	23	38.13
130305A035atm1Sa138	Alpha spiked (^{241}Am)	55	95	31	48.61
130307A035atm1Sa139	Alpha spiked (^{241}Am)	55	92	25	29.78
130308A035atm1Sa140	Alpha spiked (^{241}Am)	55	120	26	46.08
130310A035atm1Sa141	Alpha spiked (^{241}Am)	55	103	20	47.2

Table 4.4: Runs at temperature 30 ^{o}C used in data analysis

Run number	Run type	Pre-amp gain, dB	Total number of events	Number of good events	Run duration (hr)
130816A030atm1bg 006	Background	55	181	3	196.66
130316A030atm1Sn143	Neutron (^{252}Cf)	55	67	15	85.75
130320A030atm1Sn144	Neutron (^{252}Cf)	55	39	10	57.31
130322A030atm1Sn145	Neutron (^{252}Cf)	55	43	12	85.76
130326A030atm1Sn146	Neutron (^{252}Cf)	55	161	21	29.71
130327A030atm1Sn147	Neutron (^{252}Cf)	55	217	43	74.28
130330A030atm1Sn148	Neutron (^{252}Cf)	55	69	20	44.16
130401A030atm1Sn149	Neutron (^{252}Cf)	55	49	11	42.65
130403A030atm1Sn150	Neutron (^{252}Cf)	55	204	33	48.28
130126A030atm1Sa124	Alpha spiked (^{241}Am)	55	96	20	41.66
130128A030atm1Sa125	Alpha spiked (^{241}Am)	55	86	20	27.18
130129A030atm1Sa126	Alpha spiked(^{241}Am)	55	158	47	41.36
130131A030atm1Sa127	Alpha spiked (^{241}Am)	55	67	18	30.76
130201A030atm1Sa128	Alpha spiked (^{241}Am)	55	111	18	62.86
130204A030atm1Sa129	Alpha spiked (^{241}Am)	55	133	15	48.13
130206A030atm1Sa130	Alpha spiked (^{241}Am)	55	117	16	47.76
130208A030atm1Sa131	Alpha spiked (^{241}Am)	55	153	20	94.65

Table 4.5: Event rate of good events in alpha and neutron runs

Temperature (^{O}C)	Alpha events (per hr)	Neutron events (per hr)	Background events (per hr)
30	0.44 ± 0.03	0.35 ± 0.02	0.01 ± 0.009
35	0.60 ± 0.05	0.72 ± 0.06	0.03 ± 0.010
40	0.73 ± 0.06	0.82 ± 0.06	0.05 ±0.023
45	0.83 ± 0.06	0.60 ± 0.05	0.10 ± 0.074

In general, the event rates increase when increasing the temperature for a constant active mass of detector liquid. This means the event rate depends not only on temperature but also on the active mass of the detector. In this experiment, gel samples of different mass were used but with the same size of the liquid droplet. This experiment was destructive in nature and many droplets were lost while cutting the gel sample. So it was difficult to measure accurately the mass of the active liquid in each run.

4.2 Data analysis

4.2.1 Signal analysis

The main objectives of the signal analysis is to look for a possible correlation between the droplet sizes with its signal and to determine the difference between the signals produced by neutrons and those produced by alpha particles in different frequency regions. Mainly, it focused on observed and analyzed Fast Fourier Transform (FFT) of the signal in low, medium and high frequency regions to find the difference between the neutron and alpha-induced signals. It is believed that the alpha-induced signals are louder than those of neutron-induced signals [1, 48]. It was found that the signals in both cases were concentrated, with very high modulation at the early moments. The signal had a fast rise at the beginning and then fell slowly like a damped oscillation, as shown in figure 4.7. A signal started with a fast rise; attained a maximum within the first 20−40 μs,

followed by a series of slower oscillations. The first part of the pressure signal is related to the rapid growth of the vaporizing bubbles, whereas a slow component is emitted when the entire droplet has evaporated into a large ringing bubble, resulting in damped oscillations [49].

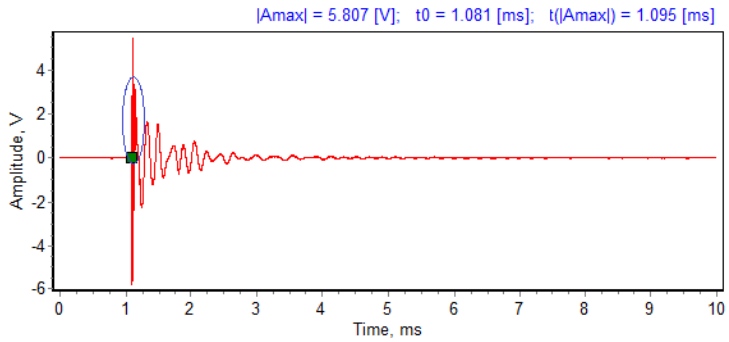

Figure 4.7: Waveform of a typical event due to droplet burst. The blue mark on the waveform shows the fast rise at the beginning of the pulse**.**

To analyze the signal, the Alazar plug in the file was converted into an ASCII/text file having two columns, with the time in the first column and the amplitude in the second column. Waveform-image software was developed in 'ROOT' as well as in MATLAB for determining t_0, t_{max}, and the absolute maximum amplitude and also to calculate the FFT power spectrum of the signal. Here t_0 is the time in which the signal begins and t_{max} is the time in which the amplitude of the signal is at the maximum value.

Later, all waveforms and corresponding live event image frames (event-by-event) were investigated. It was observed that the waveform sometimes acquired a double or triple pulse even for a very clear phase transition, as shown in figure 4.8. Tests are in progress to find the cause of such behavior, obtained in both underground as well as in laboratory experiments.

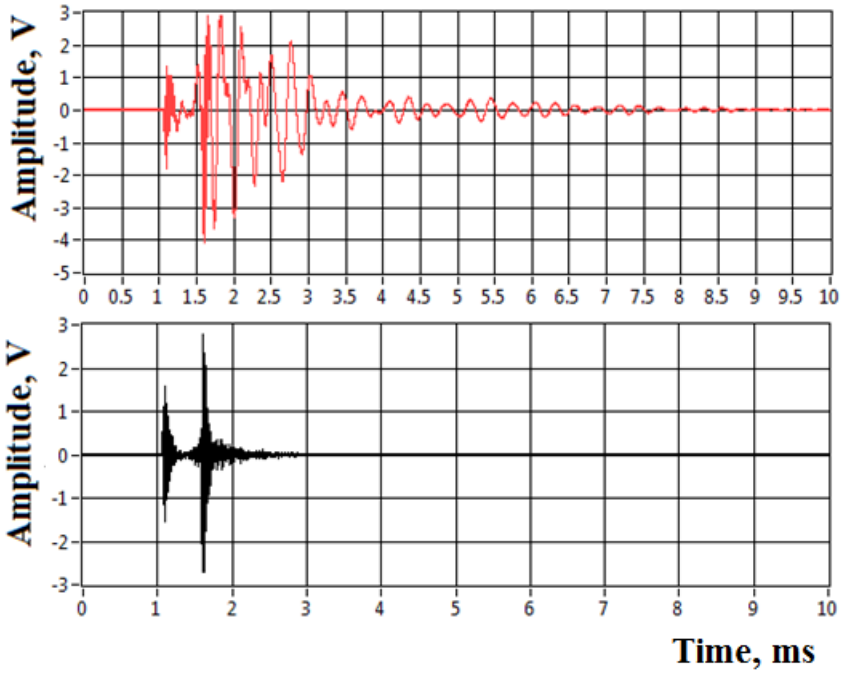

Figure 4.8: One of the examples of strange waveforms observed in clear phase transition (top) raw signal and (bottom) filtered signal using a high pass (18 kHz) filter.

4.2.2 Filters: low pass, high pass, band pass

A band pass filter on LABVIEW was used for the data analysis. Different types of filters were developed in different softwares such as MATLAB, ROOT, and LABVIEW. The regular PICASSO piezoelectric sensor was used with resonance frequency around 150 kHz. The response of the filter is maximally flat in the pass band, but has a somehow slow roll-off. In general, the design of a filter seeks to make the roll-off as narrow as possible. One important point is that a flat response in the pass band is more important than a steep roll- off to get all frequencies in the pass band represented equally.

The data analysis started by using 18 kHz high-pass Butterworth filter but the processing result did not improve the discrimination between alphas and neutrons (there were no peaks in amplitude analysis). So, the 180−300 kHz band pass filter and the 100 kHz high pass filter were chosen. All signals were filtered within the region between F_{lower} = 100 kHz and F_{upper} = 300 kHz. All low frequency vibrations, audible/acoustic

noise as well as high frequency electronics noise were cut off and the desired frequencies for the 2 MHz sampling rate of the DAQ were passed through. Further, a complex filter (nRC+ nCR) was applied to the data as well. Here n indicates the order of the filter. The construction of this type of filter is shown in figure 4.9.

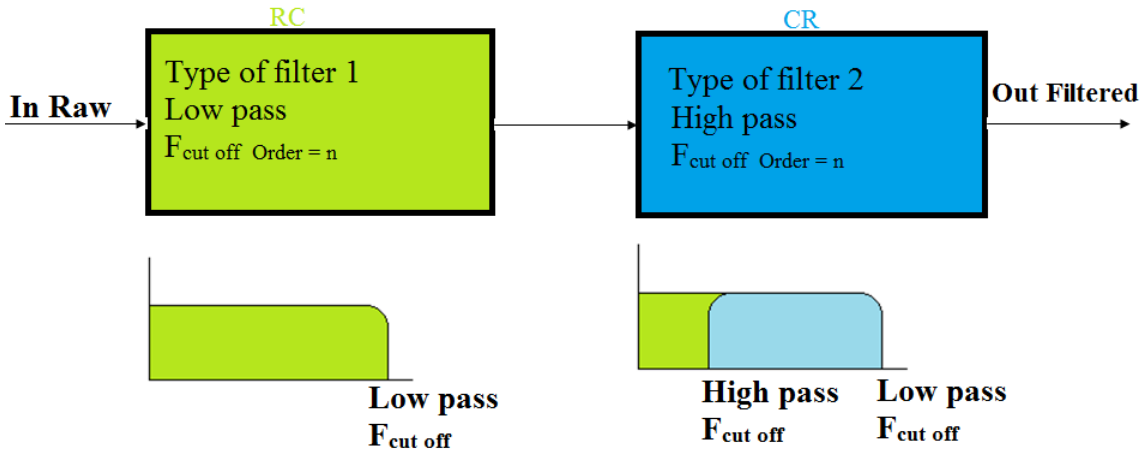

Figure 4.9: Construction of nRC+ nCR filter, n indicates order of filter. Types 1 and 2 indicate different filters such as Butterworth and Chebyshev with different frequency cut offs.

4.2.3 AVar and PVar

The important information about the primary event recorded by the piezoelectric transducer is the intensity and the frequency content of the acoustic signal. Data analysis variable to discriminate various background particle induced events as well as non-particle events are constructed based on this information. The maximum amplitude and amplitudes of the signal within the pulse duration provides basic information on the energy deposited during the nucleation process. A more precise way of presenting the results is in terms of AVar and power, named as PVar. The variable PVar, developed by G. Giroux and M.C. Piro at the Université de Montréal, is a measure of the integrated sound intensity of the fast component of the event signal. To construct PVar, first a band

pass filter is used to cut off unwanted low and high frequencies. The AVar and PVar are expressed mathematically as,

$$\text{AVar}=\log_{10}\left(\sum_i A_i\right) \tag{5.1}$$

$$\text{PVar}=\log_{10}\left(\sum_i A_i^2\right) \tag{5.2}$$

where A_i is the amplitude of the digitized acoustic signal in volts, at the i_{th} time bin and the summation extends over the duration of the signal.

4.2.4 Power spectrum

The power spectrum of the Fast Fourier Transform (FFT) of the acoustic signal is another constructed variable used in data analysis to discriminate different particle-induced signals as well as background noise-induced signals. Firstly, the FFT of particle-induced signals (alpha and neutron) in different frequency regions were studied. The average FFT of particle-induced signals in different frequency regions were also studied. The power spectrum not only gives information about dominant and interesting frequency regions, but also helps to design digital filters that are suited to data analysis. The average FFT due to phase transition at temperature 35 ^{o}C is shown in figure 4.10. It is seen from this spectrum that the region above 100 kHz to 300 kHz is interesting.

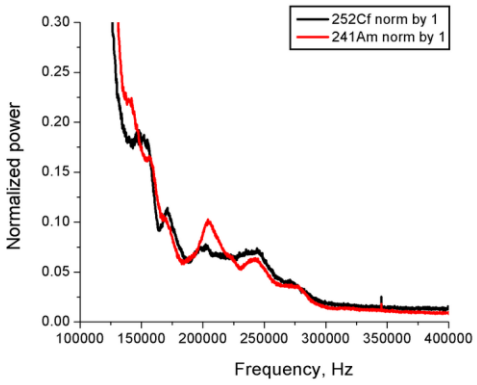

Figure 4.10: The normalized average power spectrum. All events due to phase transition at 35 ^{o}C are used to get the average value.

Chapter 5

5 Measurements of droplet and bubble sizes

The experiment started with the measurement of the droplet size (diameter) and its corresponding bubble size after the phase transition. The main purpose of these measurements is to find the actual increase in size of the droplet during the phase transition. Another purpose is to check and find a possible correlation between the droplet size and the absolute maximum amplitude of the signal at various temperatures and to see if the increase of size of the droplet depends on the temperature due to interaction with alpha-particles and neutrons.

5.1 Method

To measure the actual diameter of the droplet and the corresponding bubble, a small gel sample of approximately $1.8 \times 1.8 \times 0.7\ cm^3$ was prepared. Fresh gel (prepared at Université de Montréal) was used. The sample gel is placed on the petri dish (named as cavity) resting at the top of a piezoelectric transducer. Two digital cameras, an Infinity camera with resolution 640 × 480 and frame rate of 15 frames per second and a DMK-the Image Source camera, with high resolution of 2500 × 1980, and of frame rate of 6 frames per second, were used to take the images of the droplets and the bubbles, respectively. The cameras were calibrated by imaging a known length of 1 mm separation from a standard ruler. The distance between the scales was measured in pixels and the calibration constant was determined in units of mm per pixel. While calibrating the camera, the focal plane on the ruler was the same as for the gel sample. A schematic of the experimental set-up is shown in figure 5.1.

5.2 Ratio of bubble diameter to droplet diameter (R)

To measure the size of the droplets and the corresponding bubble, each clearly good event's image frame and the previous image frame were analyzed carefully. It is difficult to track and measure the size of the droplet that turns into the bubble whereas the bubble produced by the phase transition is highly visible and quite easily measured. GIMP2 and Microsoft paint were used to measure the size of the droplet and the bubble. For precise calculations, perfect spherical droplets and bubbles were measured and elliptical shape droplets and bubbles were discarded. The vertical and horizontal diameter of each droplet and bubble were measured twice and the average readings were taken.

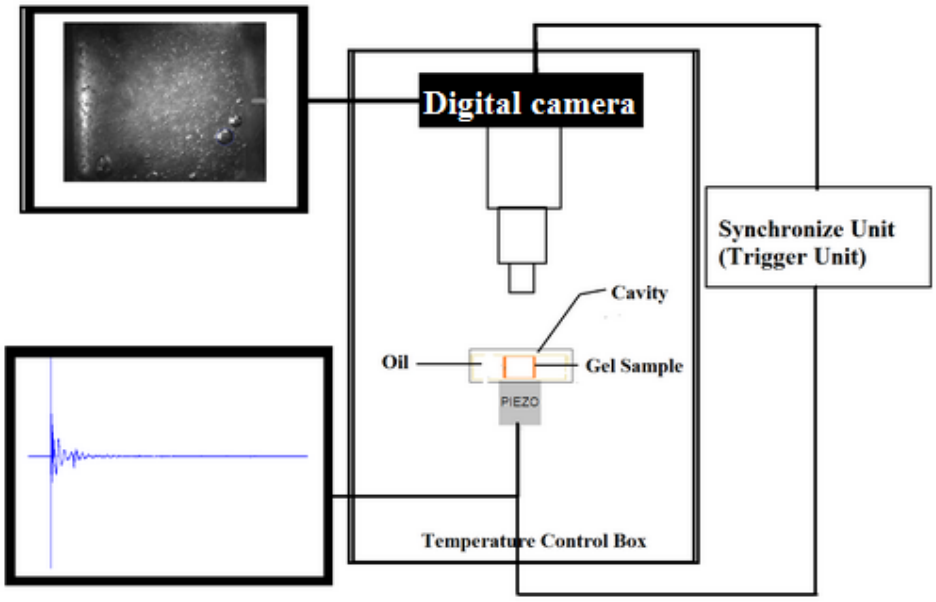

Figure 5.1: Experimental design to measure the droplet, bubble diameters and the waveform produced due to phase transitions.

The measured values of the size of the droplets and the bubbles as well as the corresponding absolute maximum amplitude of the signal were tabulated; then the mean bubble to droplet diameter ratios were calculated. For the calculations of droplet and bubble diameters, approximately 400 data points were obtained. The diameters of the

droplet and its corresponding bubble at various temperatures such as 30 ^{o}C, 35 ^{o}C, 40 ^{o}C and 45 ^{o}C were measured. Sample image frames showing the droplet distribution and the bubble formation due to phase transition and corresponding waveform are shown in figure 5.2.

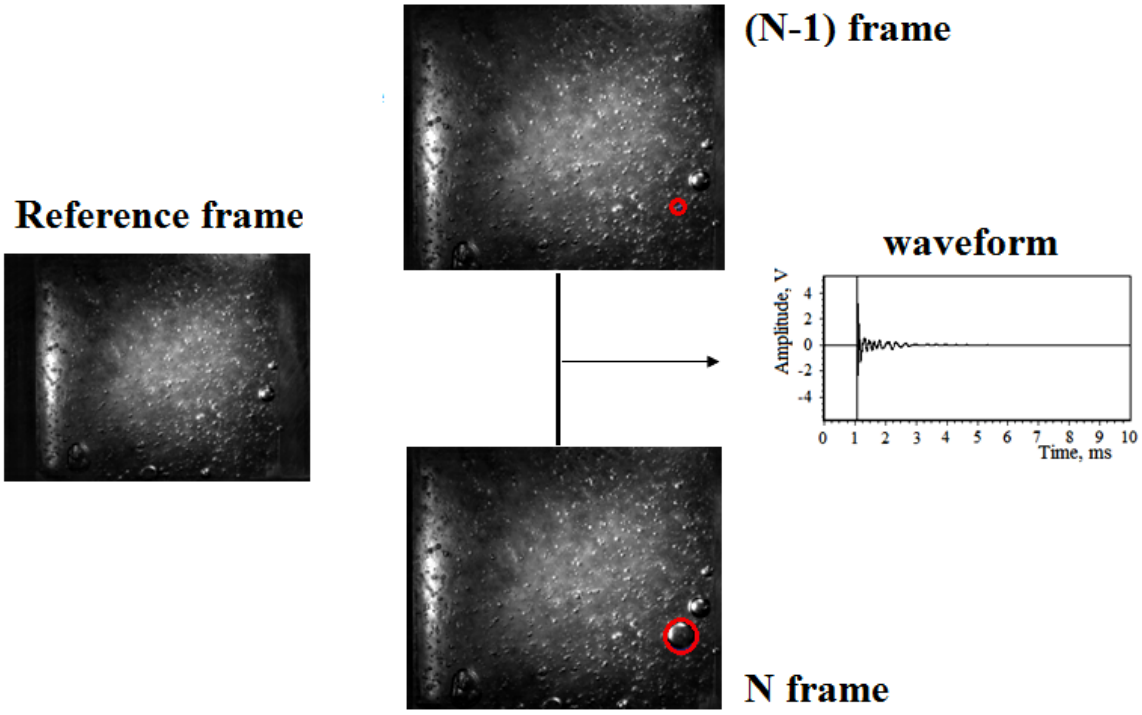

Figure 5.2: Reference image frames (left) and Acoustic waveform produced due to droplet burst (right).

5.3 Increase of the size of a droplet interacting with background particles

There is a very interesting question about the detector (Freon droplet) concerning the sensitivity and increase of size due to interaction with various background particles. One of the main advantages of the PICASSO detector is that it is insensitive to gamma rays below 55℃. All data were taken below 50 ^{o}C to avoid events induced by gamma rays. The interest was to indentify whether the increase of size of droplet depends on various background particles and temperature or not. Mainly this focused on alpha-particles and

neutrons. To achieve this propose, the spherical droplet and corresponding bubble diameters were measured in each run separately. More than 50 data points were taken in each case for good statistics. The ratios of bubble diameter to droplet diameter in alpha and neutron runs at various temperatures were tabulated and then calculated the mean ratio of bubbles diameters to droplets diameters at different temperatures. Tables 5.1 and 5.2 represent examples of measurement in alpha and neutron runs with uncertainty ±5 μm at 30 ^{o}C respectively. The Butterworth band pass (180-300 kHz) filter of order 5 was used to get filtered amplitude.

Table 5.1: Droplet diameter, bubble diameter and maximum amplitude of signal at 30 ^{o}C in alpha run

Droplet diameter, μm	Bubble diameter, μm	R	$\|A_{max}\|$, V (Raw)	$\|A_{max}\|$, V (Filtered)
268.25	1794.50	6.68	3.61	0.17
388.50	1979.50	5.09	3.55	0.29
425.50	2257.00	5.30	4.75	0.36
185.00	869.50	4.70	1.82	0.13
342.25	1813.00	5.29	3.53	0.32
148.00	925.00	6.25	3.06	0.20
203.50	1128.50	5.54	2.93	0.30
314.50	1702.00	5.41	0.72	0.17
175.75	999.00	5.68	4.26	0.19
259.00	1341.30	5.17	3.21	0.10
222.00	1591.00	7.16	5.23	0.21
222.00	1258.00	5.66	7.61	0.36

360.75	2016.50	5.58	1.71	0.35
166.50	814.00	4.88	1.82	0.24
231.25	1202.50	5.20	3.80	0.28
249.75	1239.50	4.96	2.60	0.21
166.50	906.50	5.44	1.56	0.16
314.50	1683.50	5.35	5.03	0.24
203.50	1073.00	5.27	4.40	0.32
203.50	1110.00	5.45	2.98	0.23
222.00	1110.00	5.00	10.7	0.51
351.50	1813.00	5.15	3.99	0.34
231.25	1332.00	5.76	1.90	0.14
277.50	1646.50	5.93	2.58	0.38
277.50	1295.00	4.66	3.15	0.28
185.00	962.00	5.20	1.83	0.16
351.50	1720.50	4.89	1.14	0.19
407.00	2201.50	5.40	0.80	0.23
277.50	1535.50	5.53	0.45	0.16
129.50	703.00	5.42	2.81	0.49
333.00	1868.50	5.61	2.25	0.12
129.50	721.50	5.57	1.37	0.23
157.25	906.50	5.76	1.84	0.34

185.00	1017.50	5.50	0.95	0.27
314.50	1776.00	5.64	0.27	0.09
194.25	1017.50	5.23	0.88	0.11
222.00	1165.50	5.25	2.67	0.36
462.50	2553.00	5.52	3.50	0.31
185.00	980.50	5.30	2.30	0.11
212.75	1036.00	4.87	4.90	0.22
185.00	1054.50	5.70	1.81	0.19
314.50	1720.50	5.47	0.62	0.21
296.00	1591.00	5.37	1.93	0.25
268.25	1554.00	5.79	3.00	0.16
370.00	1831.50	4.95	4.15	0.36
194.25	925.00	4.76	3.37	0.38
259.00	1443.00	5.57	4.02	0.25
148.00	906.50	6.12	2.15	0.23
259.00	1424.50	5.50	0.46	0.18

Table 5.2: Droplet diameter, bubble diameter and maximum amplitude of signal at 30 ^{o}C in neutron run

Droplet diameter, µm	Bubble diameter, µm	R	$\|A_{max}\|$, V (Raw)	$\|A_{max}\|$, V (Filter)
379.25	1942.50	5.12	1.08	0.12
351.50	1840.80	5.23	0.70	0.21
203.50	1045.30	5.13	0.24	0.08
351.50	1692.80	4.81	0.53	0.11
407.00	2090.50	5.13	2.60	0.23
342.25	1905.50	5.56	4.24	0.41
148.00	943.50	6.37	0.76	0.14
249.75	1267.30	5.07	0.74	0.09
249.75	1378.30	5.51	7.17	0.26
203.50	1110.00	5.45	5.76	0.29
231.25	1054.50	4.56	2.20	0.23
120.25	666.00	5.53	1.30	0.20
120.25	610.50	5.07	1.03	0.14
185.00	1184.00	6.40	0.40	0.17
286.75	1794.50	6.25	0.23	0.13
314.50	1609.50	5.11	0.41	0.17
296.00	1655.80	5.59	0.40	0.28
296.00	1507.70	5.10	0.42	0.33

240.50	1350.50	5.61	0.07	0.06
175.75	980.50	5.57	0.06	0.01
305.25	1526.30	5.00	3.13	0.05
120.25	481.00	4.00	2.30	0.10
222.00	1156.30	5.20	6.30	0.43
194.25	1258.00	6.47	4.90	0.14
240.50	1128.50	4.70	2.32	0.10
185.00	1026.80	5.55	3.44	0.20
277.50	1461.50	5.26	3.77	0.18
333.00	1683.50	5.05	5.40	0.29
166.50	851.00	5.11	1.75	0.19
166.50	814.00	4.88	1.03	0.19
203.50	1267.30	6.22	0.70	0.19
277.50	1628.00	5.86	0.48	0.11
268.25	1794.50	6.68	0.86	0.14
259.00	1359.80	5.25	2.17	0.16
351.50	1831.50	5.21	1.38	0.24
314.50	1646.50	5.23	2.96	0.31
277.50	1840.80	6.63	1.04	0.14
277.50	1683.50	6.06	0.41	0.11
185.00	1128.50	6.10	0.46	0.07

231.25	1332.00	5.76	0.50	0.18
222.00	1600.30	7.20	4.48	0.21
333.00	1979.50	5.94	3.74	0.24
277.50	1618.70	5.83	0.66	0.19
314.50	1785.30	5.67	0.38	0.15
296.00	1581.80	5.34	0.48	0.13

5.4 Correlation between droplet size and maximum amplitude of the signal

A possible correlation is being searched between the size of the droplet and the maximum amplitude of the waveform due to phase transition. In many research papers (such as [43, 50]) there have been efforts to find and explain the relationship between droplet size and the maximum amplitude of signal. To study this, some experiments required some correction factors based on their experimental design. For example, the angular correction for the relative position of the droplet with respect to the piezoelectric transducer and attenuation of the sound in the gel medium as well as the density of the gel matrix. It was found that the intensity of the sound decreases exponentially with the distance from the piezoelectric sensor.

It has already been discussed that very thin gel samples (5-7 mm) were taken and placed perpendicularly on the top of the piezoelectric sensor. Moreover, the sample gel was completely covered by the piezoelectric sensor so there is no portion of sample gel outside the piezoelectric sensor. To avoid the unnecessary correction and confusion about the data/experiment, droplets only on the surface of the gel (for the purpose of droplet-size measurement only) were taken and measured. Firstly, the spherical droplets on the surface of the gel sample were selected, which were produced by the observed phase transitions with the help of live-event image frames. That means that it was not necessary

to include some correction factors (mentioned earlier) in this experiment. In this analysis, the maximum amplitude of the signal due to the droplet burst was plotted as a function of the droplet diameter.

Chapter 6

6 Results

6.1 Droplet size distribution

First of all, it is necessary to know the droplet size distribution in the gel samples that were used in the experiment. The diameters of the droplets used separately for alpha or neutron runs were measured. The droplet size distribution in the gel samples is shown in figure 6.1. Figures 6.2 shows the droplet-size distribution in gel samples that were used in alpha and neutron runs. The average size of the droplets was found to be 242.30 ± 159.20 µm (95% C.L.).

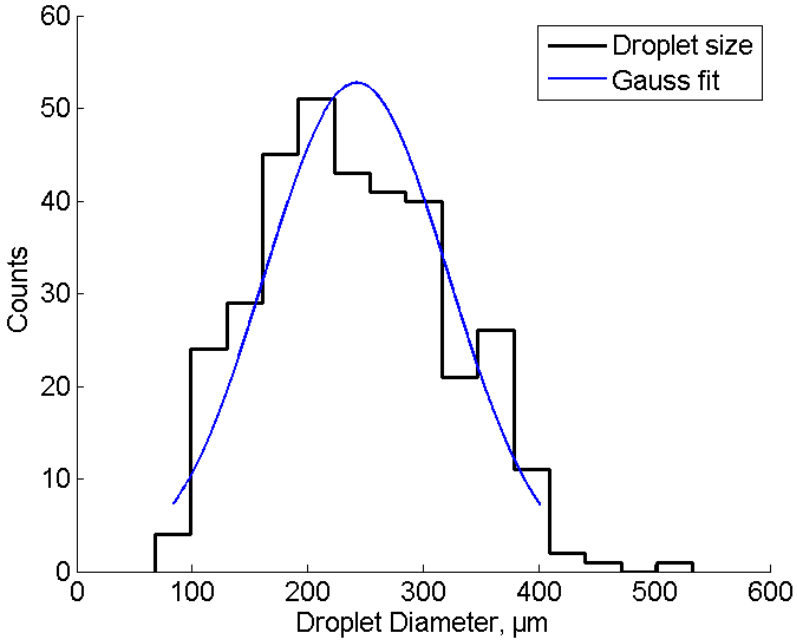

Figure 6.1: Droplet size distribution in gel samples used in both alpha and neutron runs. The measured droplets underwent phase transition.

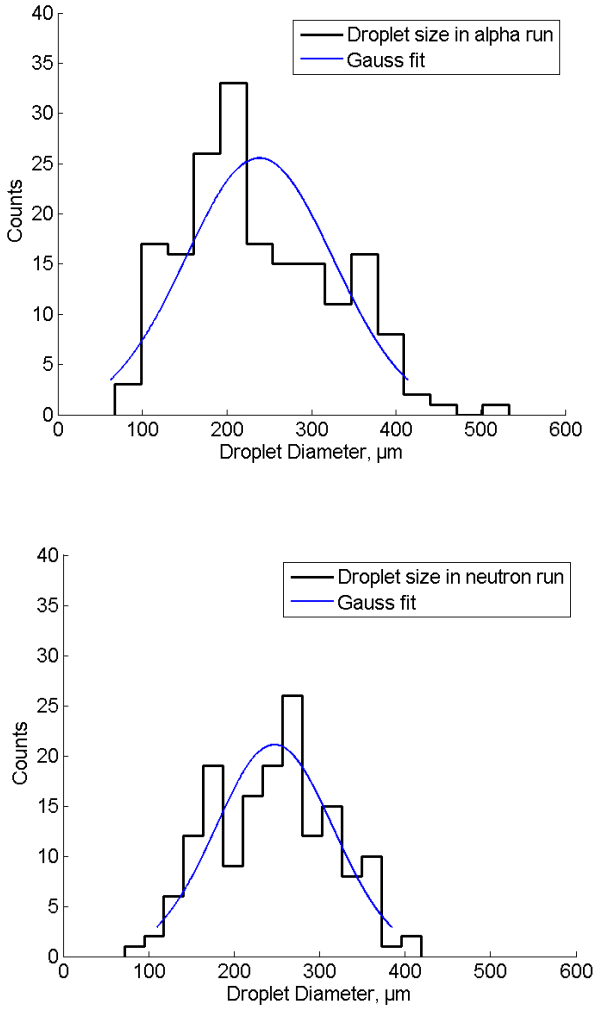

Figure 6.2: Droplet size distribution in gel samples in alpha runs (top) and in neutron runs (bottom).

6.2 Ratio of bubble diameter to droplet diameter (R)

It is interesting to know the actual increment of the size of the droplet due to phase transition. There are a few questions about the increment of size of the droplet due to phase transition such as: Is it dependent on type of interacting particles like alpha, or neutron? Is it dependent on temperature? The droplet's diameter and its corresponding bubbles in alpha and neutron runs were measured at different temperatures (30 ^{o}C, 35 ^{o}C, 40 ^{o}C and 45 ^{o}C). The calculated mean ratio of bubble diameter to droplet diameter in both alpha and neutron runs are given in table 6.1. Here n is the data points. Figure 6.3

shows the mean ratio of bubble diameter to droplet diameter in both alpha and neutron runs at different temperatures at 95% C.L.

Table 6.1: Mean ratio of bubble diameter to droplet diameter

Temperature (^{o}C)	Run	Mean ratio R (95% C.L.)	n
30	Alpha	5.44 ± 0.90	56
	Neutron	5.54 ± 1.17	45
35	Alpha	5.46 ± 1.10	39
	Neutron	5.50 ± 0.96	44
40	Alpha	5.37 ± 1.48	49
	Neutron	5.34 ± 1.10	39
45	Alpha	5.61 ± 1.24	73
	Neutron	5.64 ± 1.34	60

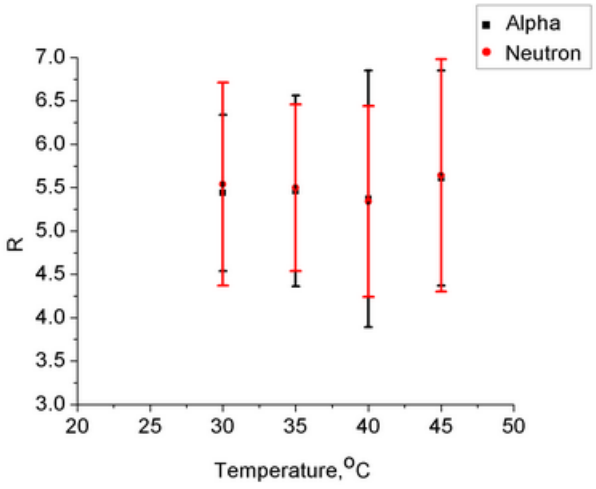

Figure 6.3: Mean bubble diameter to droplet diameter ratio at different temperatures. The error bars are at 95% C.L.

Figure 6.4 shows the histograms plots of the ratio of bubble diameter to droplet diameter in both alpha and neutron runs at temperatures of 30 ^{o}C, 35 ^{o}C, 40 ^{o}C and 45 ^{o}C respectively. It is seen that the mean ratio in both alpha and neutron runs at different temperatures are almost the same. Thus the droplet increases its size due to phase transition by approximately 5.5 times the original value or 165 times by volume. So, it is concluded that the increment of size of the droplets is independent on the type of interacting particle as well as of the temperature.

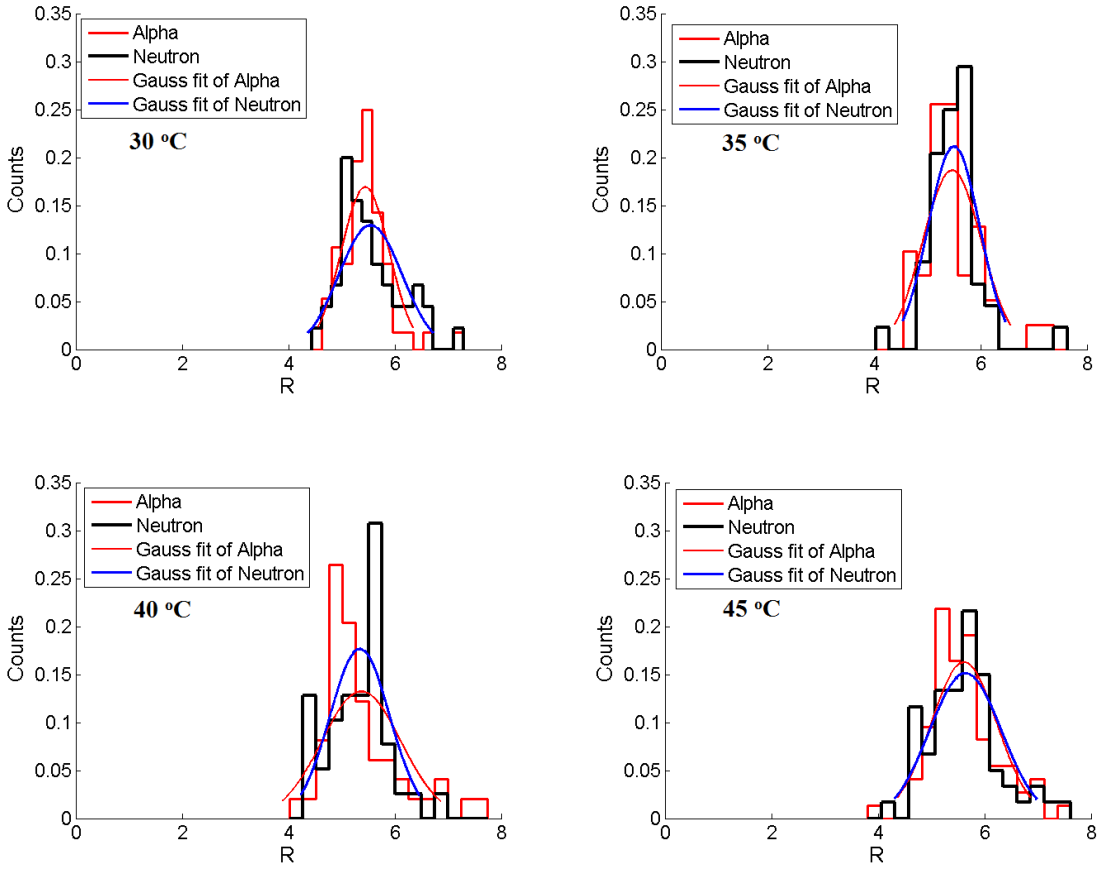

Figure 6.4: Ratio of bubble diameter to droplet diameter (R) in alpha and neutron runs undergoing phase transitions at different temperatures.

6.3 Correlation between droplets diameter and maximum amplitude of signal

It is desire to study the relationship between the droplet size and the maximum amplitude of signal due to phase transition at different temperatures. The variation of maximum amplitude of the signal, both the raw signal and the filtered signal, due to phase transition as a function of the measured droplets diameter are shown in figures 6.5, and figures 6.6 at different temperatures 30 ^{o}C to 45 ^{o}C.

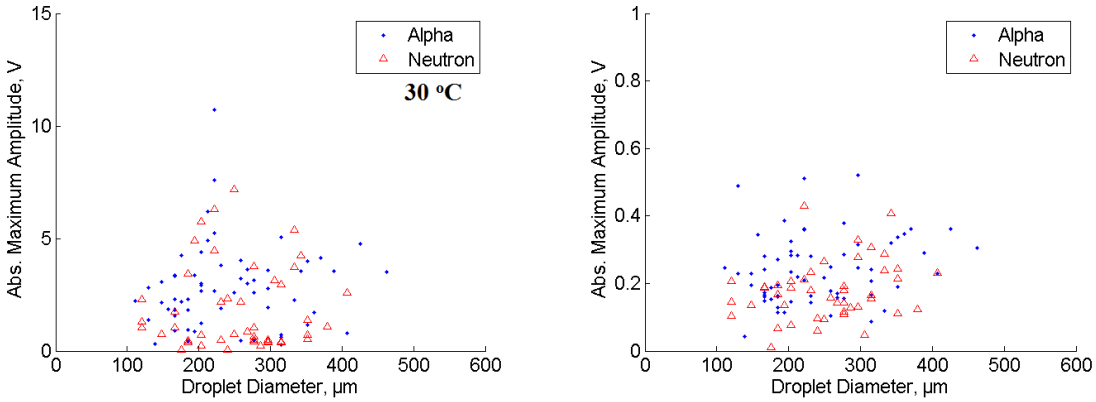

Figure 6.5: Variation of droplet diameter with maximum signal amplitude due to phase transitions at 30 ^{o}C. Left: raw signal; right: filtered signal using Butterworth band pass filter 180-300 kHz.

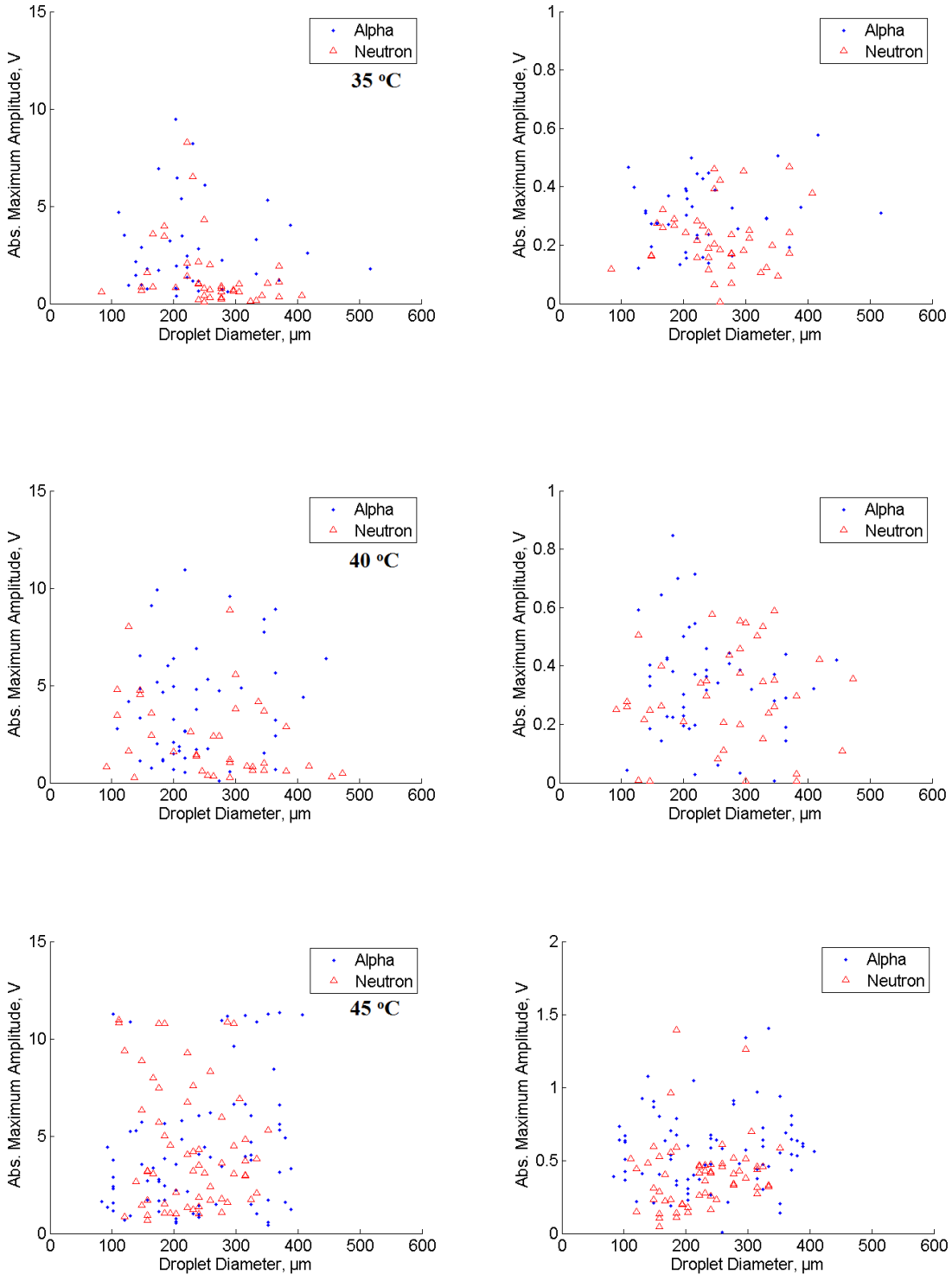

Figure 6.6: Variation of droplet diameter with maximum signal amplitude due to phase transitions at different temperatures. Left: raw signal; right: filtered signal using Butterworth band pass filter 180-300 kHz.

It is seen clearly from the plot that there is no correlation between the size of the droplet and the amplitude of the signal due to the phase transitions. For precision, only the diameter of those droplets that underwent phase transitions was measured. It was not necessary to measure the diameter of all droplets that are distributed in the gel samples. The correlation coefficient between these two parameters was also calculated. Prior to calculating the correlation coefficient between them, the distribution of these parameters were checked and found that both of them are distributed normally. The calculated correlation coefficient between droplet size and maximum amplitude of signal at different temperatures in both alpha and neutron runs are tabulated below.

Table 6.2: Correlation coefficient between droplet size and maximum amplitude of signal

Temperature (^{o}C)	Runs (particles)	Correlation Coef. (r) Raw signal	Correlation Coef. (r) Filter signal (Band Pass: 180-300 kHz)
30	Alpha	0.08	0.19
	Neutron	0.02	0.26
35	Alpha	-0.02	0.15
	Neutron	-0.27	0.08
40	Alpha	0.14	-0.17
	Neutron	-0.34	0.08
45	Alpha	0.27	-0.03
	Neutron	-0.15	0.06

It is seen from table 6.2 that the calculated correlation coefficients between these two variables are less than 0.3. In general, if the correlation coefficient between them is ±1, they have a perfectly linear relationship. If the calculated value of the correlation

coefficient between them is in the range $0.3 \leq r \leq 0.7$, they have a moderately linear relationship. But the calculated values are less than these values. In other words, the calculated values are out of the range required to establish a linear relationship. The calculated correlation coefficient between the droplet size (diameter) and the maximum amplitude of the signal due to phase transition clearly indicated that there is no correlation between these two variables at any of the temperatures considered.

6.4 Discrimination between alpha and neutron induced signals

6.4.1 Average waveforms and FFT

To discriminate between the alpha-particle and the neutron-induced signals, the signals were filtered using a 100 kHz high pass and an 180-300 kHz band pass Butterworth filter. It was found that the maximum amplitude of the signal decreased due to filtering of the frequencies below 100 kHz.

The average waveforms and FFTs of all good events due to phase transitions in both alpha and neutron runs at different temperatures (30 ^{o}C, 35 ^{o}C, 40 ^{o}C and 45 ^{o}C) were analyzed. Figure 6.7 shows the average waveforms and FFTs of good events with both alpha and neutron runs at different temperatures. It is seen from these plots that the amplitude of alpha event signals is greater than the neutron events signals at temperatures of 30 ^{o}C and 35 ^{o}C which was expected and agrees with previous underground results [1] but that, at temperature of 45 ^{o}C there was no clear separation. From the power spectrum, it was also observed that there was separation of alpha and neutron events in the frequency regions of 180-300 kHz.

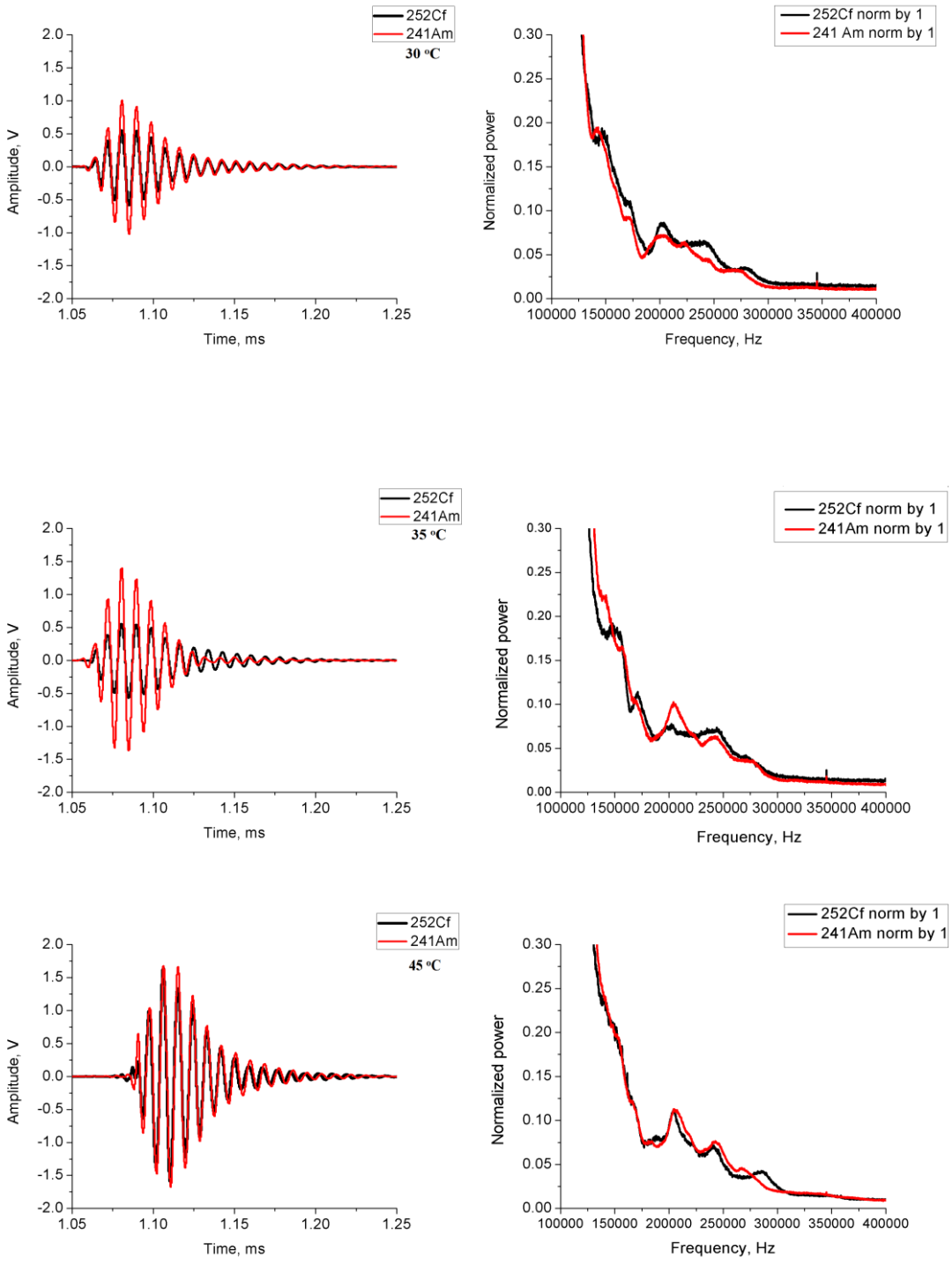

Figure 6.7: Average waveforms (left) and FFTs (right) of good events due to phase transitions at different temperatures. Butterworth high pass 100 kHz filter was used. The power is normalized and the FFT was taken in time window t_0 -10 ms.

6.4.2 Amplitude distribution

The amplitude of the signals is the main parameter to discriminate between alpha and neutron induced phase transitions in a superheated bubble detector. The distributions of the maximum amplitude of signals due to clear phase transition, confirmed by utilizing event frames, at temperatures of 30 ^{o}C, 35 ^{o}C, 40 ^{o}C and 45 ^{o}C for both alpha and neutron events are shown in figure 6.8. The counts are normalized to the total counts. Most of the alpha events overlap with neutron events and shift towards higher amplitude region which is expected and is in agreement with previous underground results [1]. At higher temperatures, the distributions shifted towards the larger amplitude region. In addition, the alpha event distribution shifted faster than the neutron event distribution.

Most of the alpha and neutron events overlap each other, especially at low temperatures and high temperatures above 40 ^{o}C. At low temperatures, around 25 ^{o}C and below, in most alpha events, only one nucleation centre was developed. Above 25 ^{o}C, if alpha emitters were located inside of the droplet, two vaporization centers should appear: the first one due to the strongly ionizing recoiling nucleus and the second one at the end of the track due to the Bragg peak. If the alpha emitters were located outside of the droplets i.e. in the detector matrix (as was the case for the ^{241}Am spiked detector) then the recoil nuclei would not contribute. But Monte Carlo simulations predict that, in both cases, fast alpha particles would be able to start nucleation above 25 ^{o}C and, with increasing temperature, the probability of multiple bubble formation on the ionizing alpha track should further increase due to the repeated occurrence of energy depositions [1]. These meet and fulfill the necessary nucleation criteria.

At higher temperatures such as 40 ^{o}C and 45 ^{o}C, the alpha component appears to be split into two peaks, with a first peak coinciding with the neutron response and the second peak, which is separated from the first one, is shifted toward higher amplitudes region. This is somehow similar to underground results [1]. The peaks or central values move toward higher amplitudes region with increased temperatures. But these shifts are not enough to show clear discrimination between alpha particle and neutron induced events.

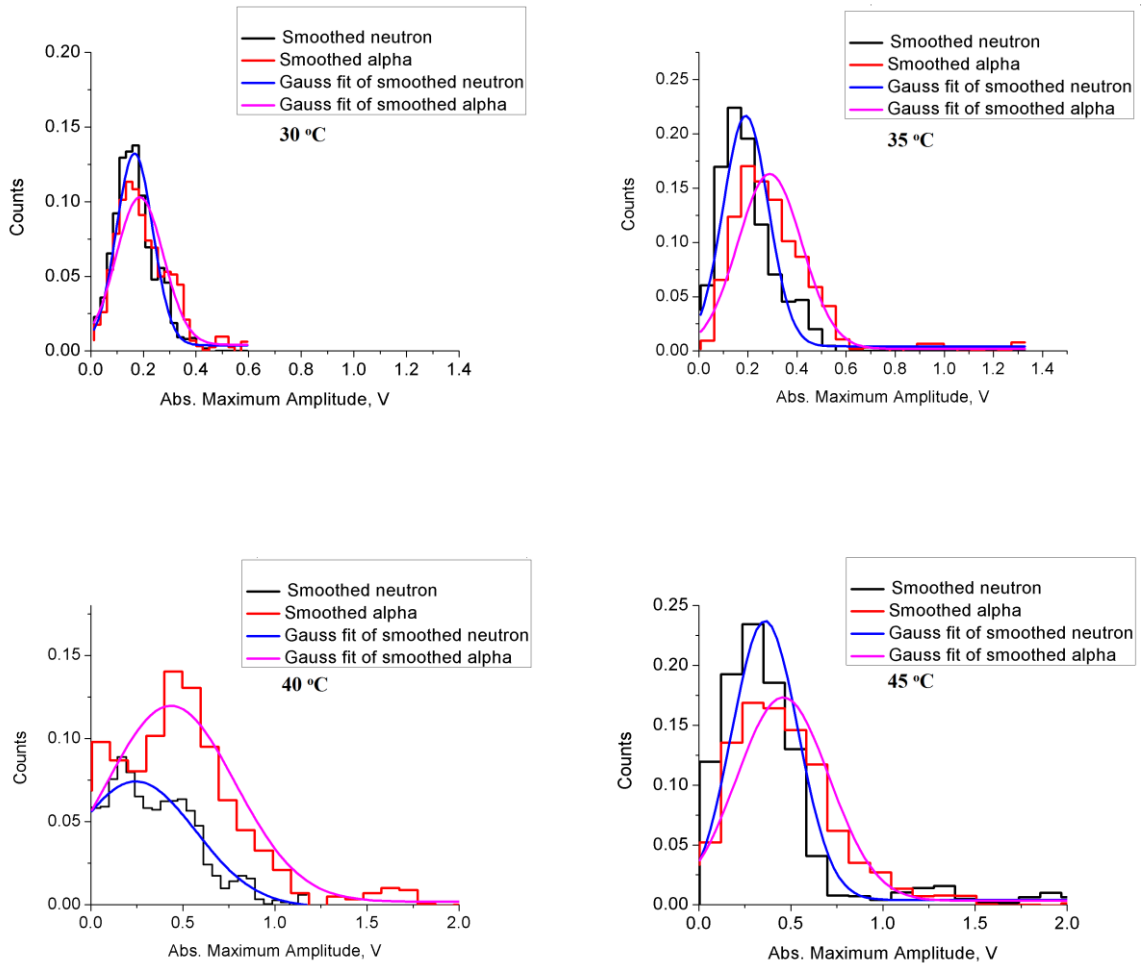

Figure 6.8: Amplitude distribution of neutron (black) and alpha particle-induced events at temperatures of 30 ^{o}C, 35 ^{o}C, 40 ^{o}C and 45 ^{o}C. Butterworth Band pass 180-300 kHz with order 5 filter was applied. The neutron data were obtained in neutron runs with a ^{252}Cf source placed close to the petri-dish and gel samples spiked with ^{241}Am were used to obtain the alpha data. Three point smoothing was applied.

It was expected that the alpha particle-induced events should be shifted more to the right to show clear discrimination, but the shifting was too slow as compared to what was observed underground [1]. This was due to two reasons: first ^{241}Am-spiked gel samples were used (outside contamination) which may not diffuse properly into the droplets, so full nucleation may not be created; and the secondly, low statistics. At higher

temperatures the amplitude was wider and the amplitude peak shifted to the right, which was in good agreement with previous results [1]. The amplitude distribution of neutron and alpha-particle induced events, obtained from both data analysis, using a band pass Butterworth filter built in MATLAB (shown in figure 6.9)

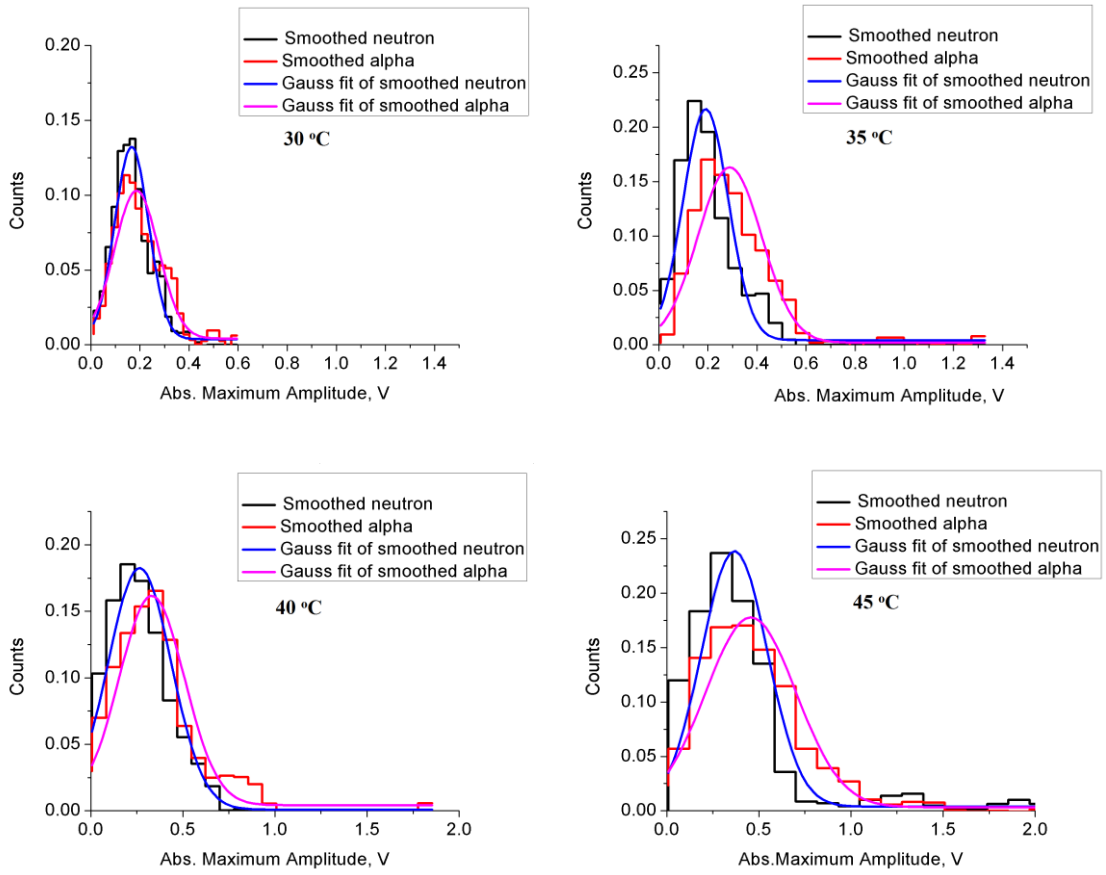

Figure 6.9: Amplitude distribution of neutron (with black border) and alpha particle-induced events at temperature of 30 ^{o}C, 35 ^{o}C, 40 ^{o}C and 45 ^{o}C. Butterworth Band pass 180-300 kHz with order 5 was applied (Built in MATLAB). The neutron data were obtained in neutron runs with a ^{252}Cf source placed close to the petri-dish and gel samples spiked with ^{241}Am were used to obtain alpha data. Three point smoothing was applied.

and LABVIEW in the same band pass region and same order showed almost the same nature. The amplitude distribution using the LABVIEW filter gave a better result than using the same type and order of filter built in MATLAB.

Further, the data were analyzed using the complex filter: 5RC + 5CR, with order 5. The resulting amplitude distribution obtained using this filter is shown in figure 6.10. This result showed better discrimination than the other filters discussed above.

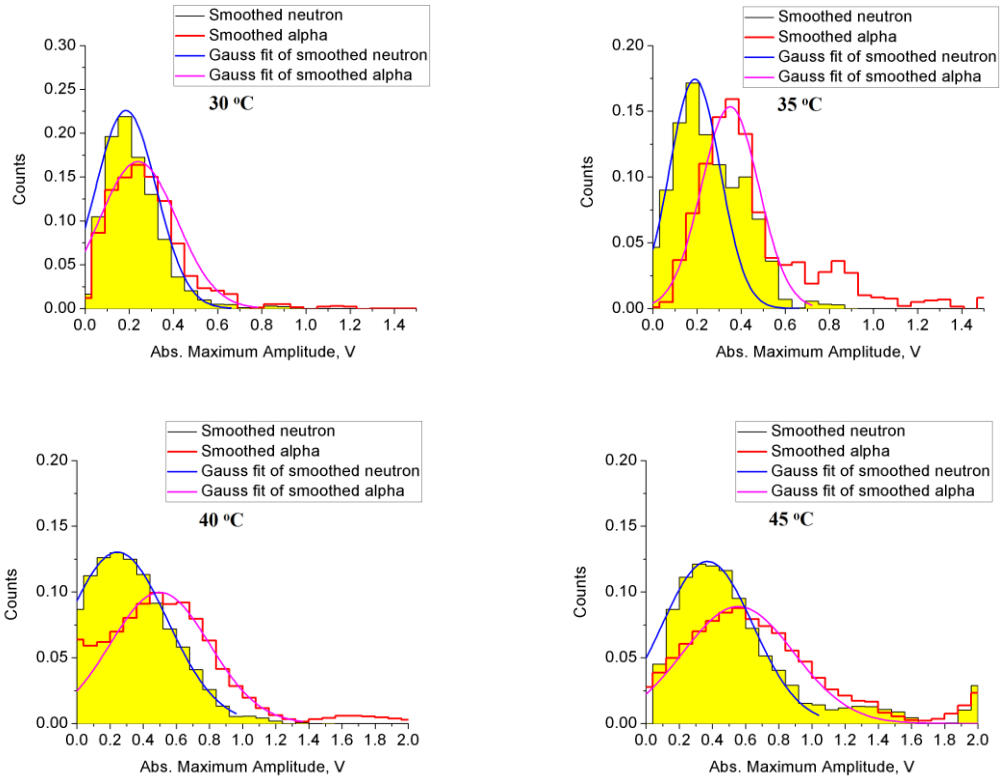

Figure 6.10: Amplitude distribution of neutron (black border) and alpha particle-induced events at temperatures of 30 ^{o}C, 35 ^{o}C, 40 ^{o}C and 45 ^{o}C. Complex Butterworth 5CR + 5RC Band pass 180-300 kHz with order 5 filters were applied. The neutron data were obtained in neutron runs with a ^{252}Cf source placed close to the petri-dish, and gel samples spiked with ^{241}Am were used to obtain alpha data. Three point smoothing was applied.

6.4.3 AVar

AVar is one of the variables developed at Laurentian University to present the results in precise way similar to PVar. PVar was/is used by our collaboration to discriminate alpha-neutron induced events. AVar is a logarithm of the sum of amplitudes of waveform taken in i^{th} time bins, where the summation extends over the duration of the waveform.

The histograms of AVar of neutron and alpha-particle induced events at different temperatures (30 ^{o}C, 35 ^{o}C, 40 ^{o}C and 45 ^{o}C) are shown in figure 6.11. In this analysis, the time duration of the waveform is 250 μs. A Butterworth band pass filter with band pass 180-300 kHz and order 5 was applied. This filter was built in LABVIEW.

Most of the alpha events overlap with neutron-induced events. Neutron-induced events reside slightly to the left of alpha-particle induced events. But a much longer shift was needed to show clear discrimination. The neutron and alpha peaks at 30 ^{o}C are 6.18 and 6.30 respectively, which is too small a difference to show clear discrimination. The peaks were shifted towards the right with increases in temperature, which was to be expected, but expected further shifts to the right to show clear discrimination between neutron and alpha-particle induced events.

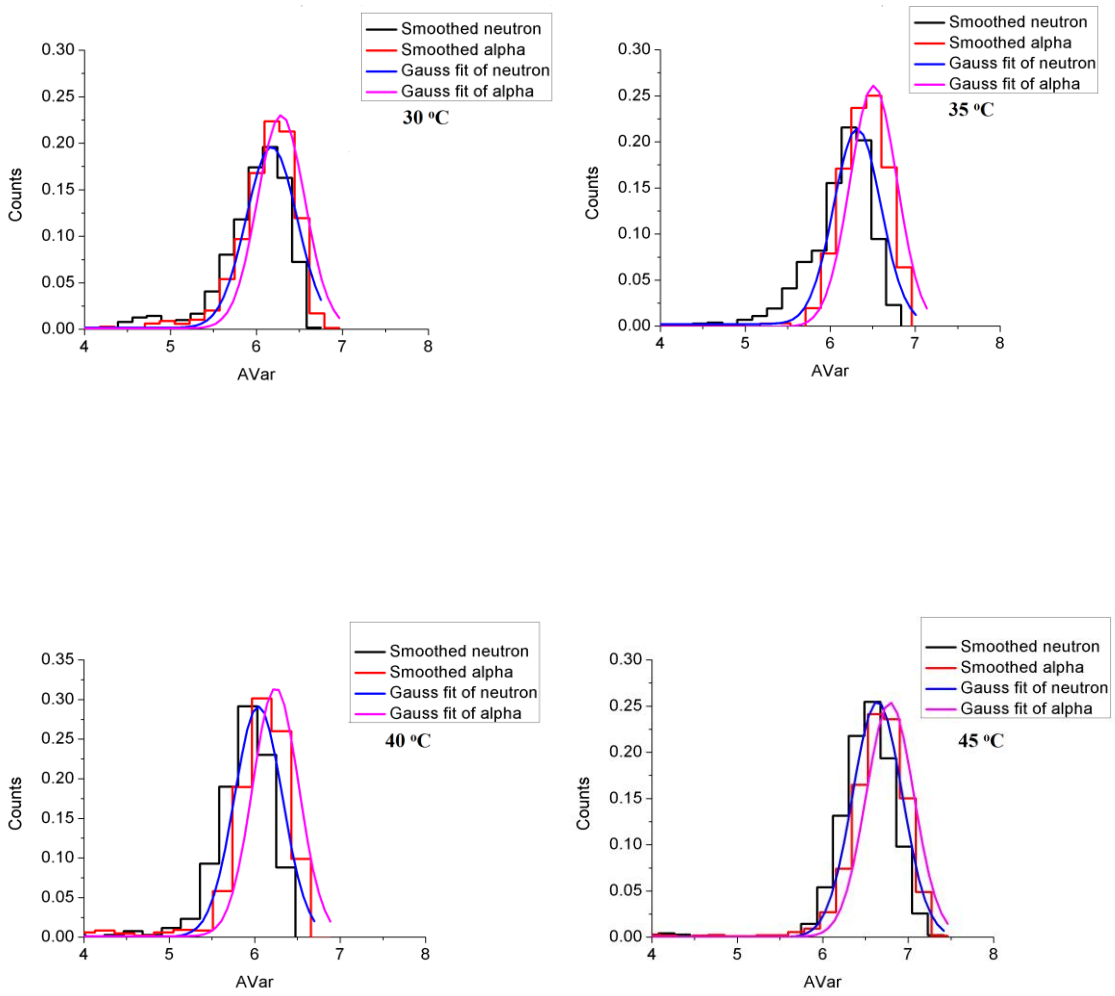

Figure 6.11: AVar of neutron (black) and alpha-particle (red) induced events at different temperatures: 30 ^{o}C, 35 ^{o}C, 40 ^{o}C and 45 ^{o}C. Butterworth band pass filter with band pass 180-300 kHz with order 5 was applied.

Chapter 7

7 Discussion and Summary

To study the response of superheated bubble detectors to alpha particles and neutrons, it is necessary to understand the working principle of the detectors, including having knowledge of the droplet size of the detectors and their effects on detecting these particles. Also, it is necessary to characterize the corresponding bubble size after phase transition and the correlation between the droplet size and the maximum amplitude of the signal. Earlier reports did not provide concrete evidence about the increase in size of the droplet during phase transition. In [35], it was mentioned that the droplet increases its volume by 500 times. Similarly, some of the articles mentioned that the droplet size increases its volume by 700 to 1000 times due to the phase transition. However, these results on the magnitude of droplet size increase due to the phase transition have not been confirmed. Furthermore, vague statements were obtained about the correlation between droplets size and the maximum amplitude of the signal. Some papers suggested that there might be a correlation between droplet size and the maximum amplitude of the signal in low frequency region only. However, these hypotheses lacked supporting proof. More interestingly, it was demonstrated that there exists no correlation between droplet size and maximum signal amplitude [43].

A possibility remains that this correlation might be associated with very low frequencies, below 18 kHz, which could not be checked in this earlier work. The dedicated experimental set up made it possible to measure the actual size of the bubbles via the help of event-by- event image frames. This research provides the measurements of the actual size of the droplet and corresponding bubble due to particle interaction. The results presented in section 6.2 showed that the droplet increased its diameter approximately 5.5 times, or 165 times by volume, during phase transition, and that this increase was independent of temperature and of the type of interacting particle. This result was one of the main findings of the research presented here.

It is clear from figures 6.5 and 6.6 and table 6.2, that there was no correlation between droplet size (diameter) and the maximum amplitude of the signal (raw signal or filtered signal). Moreover, the calculated Pearson correlation coefficient, table 6.2, between these two variables, confirmed those results. It was observed from these distributions that some droplets of smaller size seem to be producing higher amplitude signals than the larger size droplets. However, no generalization could be made regarding small droplets produced a more powerful and louder sound than larger droplets. It was expected that there may be a correlation between droplet size and maximum amplitude of filtered signal in low frequency region. This was checked using low pass filters even from 2-15 kHz, 10-25 kHz and 18 kHz high pass filters but no improvement or correlation in the analysis was observed. This was probably due to the fact of using high frequency piezoelectric sensor having resonance frequency 150 kHz.

It is possible that no correlation was observed due to factors such as attenuation effects, angle of incidence or the distance of the signal from the piezoelectric sensor. The use of very thin gel samples (7 mm thick) which covered the piezoelectric sensor as well as direct attachment meant that the incident sound wave was directly perpendicular. These considerations combined suggest that the later factors did not apply to this experiment.

Further, this study of droplet size and bubble size revealed the exact picture of the increase of droplet size due to particle interactions, which turned out to be independent of the type of interacting particle and temperature. The study also showed that there was no correlation between droplet size and maximum amplitude of signal.

Almost all data analysis variables, including PVar and AVar, were based on the amplitude of the signal. The amplitude of the signal was very important at the beginning, as the signal had a steep increase at the beginning and then decreased slowly like, a damped oscillation. The signal attained a maximum value within 20-40 μs. Figures 6.8, 6.9 and 6.10 show the maximum amplitude distribution of the alpha particles and neutron- induced events at different temperatures. However, these amplitude distributions did not show clear discrimination between alpha particles and neutron-induced events,

except at temperature of 35 ^{o}C, which has better discrimination. It was expected that the alpha particle induced events would populate the high amplitude region, but most of the events were found in the low amplitude region overlapping with neutron-induced events. There are many possible reasons as to why no clear discrimination between alpha particle and neutron induced events was observed.

PICASSO uses a model [1] to explain the physics behind the difference in signal amplitude between alpha particle and neutron-induced events. In principle, alpha particles can create multiple nucleation sites while traversing the droplet in a way that depends on the temperature, size of the droplet, and the alpha particle energy, whereas the neutron always creates a single nucleation site. But if the alpha emitters are located outside of the droplets, multiple nucleation sites may not be created. If ^{241}Am liquid is used as an alpha emitter, multiple nucleations are unlikely as it does not diffuse inside the droplet. As ^{241}Am liquid was used as an alpha emitter in alpha runs at all temperatures, this may be a possible reason of these results. A better choice would have been to use radon as an alpha emitter, as radon diffuses properly inside the droplets and multiple nucleation sites might be created. Attempts were made to use radon as an alpha source for alpha run but difficulties arose such as droplets bursting due to the warm room. While spiking with radon, it is necessary to keep the gel sample for at least 12 hours under air containing high levels of radon. During these times more than 50% of the droplets phase out or turn into bubbles before the experiment has started. Even when these spiked gel samples were used, they produced too many clustered events, which created other problems such as density effects and hence could not be considered good events, resulting in very low statistics. There were only 32 good events from five runs.

Gel samples fabricated at different times were used and found that some gel samples were not properly set and, as a result, unable to fix the droplets and bubbles formed after the phase transition. In a perfect gel sample, the droplets and the bubble formed after the phase transition are properly fixed inside the gel matrix. Sometimes white foam inside the gel sample was found and the sample did not have the proper size and shape. Such types of gel samples were used in both alpha and neutron runs at a temperature of 40 ^{o}C.

The discrimination results also depend on the choice of filters, their order as well as their construction, which were applied during data analysis. The beginning of the data analysis used an 18 kHz high pass filter. But the preliminary results did not show any discrimination. The average waveform and FFTs of all events in different frequency regions were studied to find the significant region or the proper cut off region. Filters with different order and choosing different frequency bands were checked. The Butterworth band pass filter of order 5 was found to be the best one in terms of improving discrimination. Figures 6.8, 6.9 and 6.10 showed the results of amplitude distributions using different types of filters built in different software. The amplitude distribution shown in figure 6.10 has better discrimination. It was obtained by applying the complex filter 5CR+5RC. That means the discrimination results depend on the filter applied to the signals. Moreover, the temperature range is the main other factor. The temperature above 30 ^{o}C and below 40 ^{o}C was the best temperature range for alpha-neutron discrimination in this experiment.

More data analysis tools such as PVar and AVar were also implemented in this analysis but did not show any improvements in discrimination. In principle, the discrimination should have improved at temperatures above 40 ^{o}C. However, there were probably systematic effects, not fully understood at this point, that prevented a more conclusive study of the discrimination at high temperatures.

8 References

[1] PICASSO, F. Aubin et al., New Journal of Physics **10**: 103017 (2008).

[2] http://www.amnh.org/explore/resource-collections/cosmic-horizons/profile-fritz-zwicky-s-extraordinary-vision.

[3] R. A. Freedman , W. J. Kaufman , *Universe, 8th ed*. New York, W.H. Freedman and Co. III (2007).

[4] G. Jungman, M. Kamionkowski, K. Griest, Super symmetric dark matter, Physics Reports **267**:195-373, (1996).

[5] K. G. Begeman, A.H. Broeils and R.H. Sanders, Mon. Not. R. Astron. Soc. **24** (1991) 523.

[6] J. Binney and S. Tremaine, *Galactic Dynamics* (Princeton University Press, Princeton, 1987).

[7] G. Hinshaw et al, arXiv: 1212.5226v3.

[8] Da-Ming Chen. Flux-Limited Strong Gravitational lensing and dark energy. Astronomy and Astrophysics, **418**(2):387–392 (2004).

[9] www.pha.jhu.edu/~papovich/astropics/cl0024.html.

[10] X-ray: NASA/CXC/CfA/M.Markevitchetal.; Optical: NASA/STScIMagellan/U.Arizona/D.Cloweetal.; Lensing Map: NASA/STScI; ESOWFI; Magellan/U.Arizona/D.Clowe et al.

[11] WMAP, G. Hinshaw et al., ApJS **180**: 225 (2009).

[12] S. Burles, K. Nollett, and M. Turner, Phys.Rev.D **63**: 063512 (2001).

[13] www.astro.princeton.edu/~dns/MAP/Bahcall/node16.html.

[14] S.Weinberg, Phys.Rev.Lett. **40**: 223 (1978).

[15] R.L. Davis, Phys.Lett.B, **180**: 225 (1986).

[16] G. Raffelt, to appear in proceeding of the XVthMoriond Workshop: Dark matter in Cosmology, Clocks and Test of Fundamental laws, Villars-Sur-ollon, Switzerland, January 21,1995.

[17] J. Kim and G. Carosi, arXiv: 0807. 3125 v2 [hep-ph].

[18] L. Roszkowski. *Particle Dark Matter - A Theorist's Perspective*. Pramana - Journal of Physics, **62:** (2), (2004).

[19] J. Primark, arXiv: astro-ph/9707285v2.

[20] R. Gaitskell, Annu. Rev.Nucl. Part.Sci.**54**: 315 (2004).

[21] C. Frenk and S. White, arXiv: 1205, 4882 v3.

[22] F. Halzen, D. Hooper, New Journal of Physics, **11**:105019 (2009)

[23] J. D. Zornoza, arXiv: 1204.5066.

[24] G. Bertone, Phys. Rep.405: 279 (2005).

[25] E. Baltz et al, JCAP 7, 0807: 013 (2008).

[26] VERITAS, J. Holder et al, Astropart.Phys. **25**: 391 (2006).

[27] CANGAROO, M. Olishi et al. Astropart. Phys. **30**: 47 (2008).

[28] J.D. Lewin, P.F. Smith. Astroparticle Physics **6**: 87-112 (1996).

[29] S. Archambault et al, arXiv: 1202.1240v1.

[30] J.D. Lewin, P.F. Smith. **187**(5): 203- 280 (1990).

[31] Steven J.S. Plank, *The DRIFT Dark Matter Project: Directionality, Sensitivity and Environmental Background, PhD thesis*, The University of Edinburgh (2008).

[32] M. Schumann, arXiv:1206.2169.

[33] F. Seitz, The Physics of Fluids, American Institute of Physics, **1**, 2 (1958).

[34] Ch. Peyrou, in Bubble and spark Chambers, edited by R.P. Shutt(Academic press, New York 1967).

[35] PICASSO, Barnabe`-Heider et al., Nucl. Instrum. Meth. A**555**: 180-204 (2007).

[36] R. E. Apfel, S.C. Roy and Y.C. Lo, Phys.Rev. A31: 3194 (1985).

[37] C.R. Bell, N.P. Oberle, W. Rohsenow, N. Todreas and C. Tso, Nucl.Sci. Eng., 53: 458 (1974).

[38] L.A. Hamel et al. Nucl. Instru. And Meth. in Phys.Res. A338: 91-99 (1997).

[39] PICASSO, S. Archambault et al., arXiv: 0907.0307v1.

[40] Francesco d' Errico, Nucl. Instr. Meth. B184: 229 (2001).

[41] PICASSO, public website, http://www.picassoexperiment.ca/experiment_detector.php.

[42] X. Dai and Y. Zhu, Procedure for the fabrication of 4.5L salt-less PICASSO detector, PSTR-07-012, (PICASSO Scientific/Technical Report) (2007).

[43] P. Nadeau, *Alpha-Neutron discrimination and droplet size measurements in the PICASSO experiment*, M.Sc. thesis, Laurentian University, Sudbury, ON, (2009).

[41] J.F. Ziegler and J.P. Biersack, TRIM (Transport of Ions in Matter), Version TRIM-96 in SRIM-2000 (The stopping and Range of Ions in Matter), version 2000.39 coded by D.J. Mawrick et al., copyright 1998,1999 by IBM Co.

[45] A. C. Kamaha, "Study of the Neutron Background", PICASSO collaboration internal document (2011).

[46] D.M. Mei and A. Hime , Phys. Rev.D 73:053004 (2006).

[47] M. Besnier, Simulation of alpha particle behaviour inside a C4F10 bubble (picassoweb.lps.umontreal.ca/elog/Analysis+Meetings/24).

[48] PICASSO, S. Archambault et al., arXiv:0907.0307v2.

[49] J.E. Shepherd, *Dynamics of vapour explosions: rapid evaporation and instability of butane droplets at the superheated limit,* PhD Thesis Caltech (1980).

[50] P. K. Mondal, Study of bubble size vs. pulse amp in SDD

(picassoweb.lps.umontreal.ca/elog/Weekly+Meetings/285).